MNRAS **000**, 000–000 (0000) Preprint 2 April 2021 Compiled using MNRAS LATEX style file v3.0

Deep Learning Assessment of galaxy morphology in S-PLUS Data Release 1

C. R. Bom,[1,2]★ A. Cortesi[3], G. Lucatelli[4], L. O. Dias[1], P. Schubert[1], G.B. Oliveira Schwarz[5], N. M. Cardoso[6], E. V. R. Lima[4], C. Mendes de Oliveira[4], L. Sodre Jr.[4], A.V. Smith Castelli[7,8], F. Ferrari[9], G. Damke[10], R. Overzier[11,4], A. Kanaan[12], T. Ribeiro[13], W. Schoenell[14]

[1] *Centro Brasileiro de Pesquisas Físicas, Rua Dr. Xavier Sigaud 150, CEP 22290-180, Rio de Janeiro, RJ, Brazil*
[2] *Centro Federal de Educação Tecnológica Celso Suckow da Fonseca, Rodovia Mário Covas, lote J2, quadra J, CEP 23810-000, Itaguaí, RJ, Brazil*
[3] *Valongo Observatory, Federal University of Rio de Janeiro, Ladeira Pedro Antonio 43, Saude Rio de Janeiro, RJ, 20080-090, Brazil*
[4] *Universidade de São Paulo, IAG, Rua do Mato 1225, Sao Paulo, SP, Brazil*
[5] *Universidade Presbiteriana Mackenzie, R. da Consolação, 930 - Consolação, São Paulo, Brazil*
[6] *Escola Politécnica, Universidade de São Paulo, Av. Prof. Luciano*
[7] *Facultad de Ciencias Astrónomicas y Geofísicas, UNLP, Argentina*
[8] *Instituto de Astrofśica de La Plata, CONICET–UNLP, Argentina*
[9] *Universidade Federal do Rio Grande, Instituto de Matemática, Estatística e Física, 8 km Itália Av., Rio Grande, RS, Brazil*
[10] *Instituto de Investigación Multidisciplinar en Ciencia y Tecnología, Universidad de La Serena, Raúl Bitrán 1305, La Serena, Chile*
[11] *Observatório Nacional, Rua General José Cristino, 77, São Cristóvão, 20921-400, Rio de Janeiro, RJ, Brazil*
[12] *Departamento de Física, Universidade Federal de Santa Catarina, Florianópolis, SC, 88040-900, Brazil*
[13] *Departamento de Astronomia, Instituto de Física, Universidade Federal do Rio Grande do Sul (UFRGS), Av. Bento Goncalves 9500.*
[14] *NOAO, P.O. Box 26732, Tucson, AZ 85726*

2 April 2021

ABSTRACT

The morphological classification of galaxies is a relevant probe for galaxy evolution and unveils its connection with cosmological structure formation. To this scope, it is fundamental to recover galaxy morphologies over large areas of the sky. In this paper, we present a morphological catalogue for galaxies in the Stripe-82 area, observed with S-PLUS, till a magnitude limit of $r \leq 17$, using the state-of-the-art of Convolutional Neural Networks (CNNs) for computer vision. This analysis will then be extended to the whole S-PLUS survey data, covering $\simeq 9300\ deg^2$ of the celestial sphere in twelve optical bands.

We find that the network's performance increases with 5 broad bands and additional 3 narrow bands compared to our baseline with 3 bands. However, it does lose performance when using the full 12 band image information. Nevertheless, the best result is achieved with 3 bands, when using pre-trained network weights in an ImageNet dataset. These results enhance the importance of previous knowledge in the neural network weights based on training in non related extensive datasets. Thus, we release a model pre-trained in several bands that could be adapted to other surveys. We develop a catalogue of 3274 galaxies in Stripe-82 that are not presented in Galaxy Zoo 1 (GZ1). We also add classification to 4686 galaxies considered ambiguous in GZ1 dataset. Finally, we present a prospect of a novel way to take advantage of 12 bands information for morphological classification using multiband morphometric features. The morphological catalogues are publicly available.

Key words: galaxies: fundamental parameters – galaxies: structure – techniques: image processing – methods: miscellaneous – surveys

1 INTRODUCTION

Galaxy morphology is the study of the shapes and structural properties of galaxies. For centuries, there have been many definitions of different classes of galaxies, in an attempt to understand the physical nature behind the differences in galaxy shapes (e.g. Zwicky 1940; Vaucouleurs 1959; van den Bergh 1998 and references therein). Since the first galaxy classification schemes created from the 18^{th} century on, by Sir William Herschel, his son Sir John Herschel, Curtis, Edwin Hubble, among others, it was already rec-

★ E-mail: debom@cbpf.br (CRB)

ognized that many galaxies (by then called nebulae) had spiral arms while others had smooth and elliptical appearance (e.g. Herschel 1864). Even today, when many other more modern galaxy classification schemes are available, with a wealth of sub-types (e.g. Borne et al. 1999), the main classes, for luminous objects, remain as Spiral (S) and Elliptical (E) galaxies.

Morphological differences often reflect the presence of contrasting stellar populations (Sánchez et al. 2007) and stellar kinematics (Edelen 1969; Wang et al. 2020), which are connected to the galaxies' masses and environments (Calvi et al. 2012; Crossett et al. 2014; Sarkar & Pandey 2020; Wu 2020). For example, S galaxies are characterized by the presence of a disk, indicating rotationally supported stellar kinematics, and they generally present blue spiral arms, with newly born stars. Furthermore, S galaxies must have access to a reservoir of gas to maintain their star-formation activity. In contrast, E galaxies have, in general, more smooth morphologies and are pressure-supported systems (though some of them seem to display rotation; e.g., Bernardi et al. 2019), as a result of a sequence of, mainly, minor mergers (e.g. Kormendy et al. 2009; Naab et al. 2009; Forbes et al. 2011). As a global rule, massive galaxies evolve faster than the less massive ones, but this behaviour is less pronounced when morphology is taken into account (Camps-Fariña et al. 2020). This shows that morphology is an evolutionary key factor and, as a consequence, the study of galaxies' morphologies allows understanding galaxy evolution throughout cosmic times (e.g. Shao et al. 2015).

Sky surveys in three or more bands have become widespread in the last decades, which have brought a revolution, in particular, of the fields of large scale structure and galaxy formation and evolution. Most notably, since Sloan Digital Sky Survey (SDSS; York et al. 2000), studies evolved from using hundreds to hundreds of thousands and millions of astronomical objects, with the exploration of large volumes of the sky at once, and the massive use of automatically obtained parameters. The methods used to perform the classifications are also quite diverse, going from human classification of specialists (Nair & Abraham 2010; Ann et al. 2015), to citizen science (Lintott et al. 2008, 2010; Willett et al. 2013; Simmons et al. 2017), or to numerical estimation of morphology from galaxies' properties (Spiekermann 1992; Storrie-Lombardi et al. 1992; Walmsley et al. 2020). Nevertheless, all these methods share a common problem: the image quality decreases as galaxies become fainter and farther away, and it is highly dependent on the resolution of the instrument, compromising a correct classification (e.g. Pović et al. 2015). In order to mitigate these issues, methods based on the Principal Component Analysis (PCA; Kelly & McKay 2004; Wjeisinghe et al. 2010) and/or Machine Learning (ML), are also used to improve galaxy classification (de la Calleja & Fuentes 2004; Yamauchi et al. 2005; Huertas-Company et al. 2008; Banerji et al. 2010; Domínguez Sánchez et al. 2018; Wu et al. 2019; Clarke et al. 2020; Barchi et al. 2020). The prospect is for fast progress in the next years due to Legacy Survey of Space and Time (LSST; Tyson 2002; Axelrod 2006) in the Vera C. Rubin Observatory, The Nancy Grace roman Space Telescope (Gehrels & and 2015) and many others. The volume of data involved makes it unfeasible to perform galaxy morphology using citizen science efforts only.

Thus, ML methods appeared as excellent tools to analyse Astronomical data, given that they can acquire valid information from various data sets and assist in the process of decision-making. As successful examples, ML techniques have been used to detect gravitational lenses, interacting galaxies, and classify quasars (to mention a few examples), on top of performing morphological type classification, as previously mentioned (Freeman et al. 2013; Shamir et al. 2013; Bom et al. 2015, 2017; Ostrovski et al. 2017; Ma et al. 2019; Metcalf et al. 2019; Knabel et al. 2020). In the last decade, a subfield of ML, known as Deep Learning (DL), has emerged as the main technique for computer vision applications, including classification, facial recognition (Lu et al. 2017), speech detection and characterization (Abdel-Hamid et al. 2014; Vecchiotti et al. 2018), object segmentation, music classification (Choi et al. 2017), as well as medical prognostics (Li et al. 2018) and diagnostics (Hannun et al. 2019). Therefore, DL techniques are useful to a wide range of multidisciplinary fields, including Astronomy.

In the astronomical specific field, DL allows the development of models that can process complex and minimally processed (even raw) data from various sources to extract relevant features that can be effectively linked to other properties of interest. In particular, Deep Neural Networks (DNNs) are high-performance data-driven models that can even exceed humans in classification tasks (Metcalf et al. 2019). A number of recent works have demonstrated that DNNs can be used to identify morphological features in raw images, with minimal intervention from humans (Glazebrook et al. 2017; Farias et al. 2020; Hausen & Robertson 2020; Lanusse et al. 2018b; Cheng et al. 2019; Jacobs et al. 2019; Petrillo et al. 2019a,b; Metcalf et al. 2019; Madireddy et al. 2019; Barchi et al. 2020).

In this paper, we present a morphological classification of galaxies into Ss and Es, using the new Southern Photometric Local Universe Survey (S-PLUS; Mendes de Oliveira et al. 2019). The First Data Release (DR1) of S-PLUS covers the area of Stripe-82 which has been extensively explored by several other surveys and, in particular, by SDSS and GZ1. The previous results obtained for GZ1 over the area of Stripe-82 for SDSS, are used as true tables. S-PLUS is a 12 band imaging survey covering ~ 9300 deg^2 of the Southern sky, recently described by Mendes de Oliveira et al. (2019). We aim to test the effect of the 12-bands compared to the broad bands for classification. We also test the use of some of the state-of-the-art DL architectures for computer vision and evaluate how important it is to start our training with the neural network weights already optimized in another dataset. Lastly, we present our morphological classification catalogue containing 3274 galaxies that were not presented in previous GZ1 releases and classification for a set of 4686 galaxies considered ambiguous in GZ1 catalogue. The catalogues and additional analysis plots are made publicly available [1].

This paper is organized as follows. Section 2 presents the data and the definition of the different samples used in the DL process. Section 3 and Section 4 present the DL models and the morphological analysis techniques used in this work. Section 5 give the details of the training and validation process and Section 6 presents the results as well as a check of our method. There, we also show the concordance that exists between our proposed galaxy morphological classification and spectral types (as obtained from photo-z template fitting codes). We also present correlations of morphologies with the output parameters from 2D decomposition codes such as Morfometryka (Ferrari et al. 2015) and Galfit (Peng et al. 2002) (using parameters such as concentration and clumpiness). Finally, in Section 7 we present a summary and the discussion of our work and the concluding remarks.

[1] The catalogue can be downloaded in https://github.com/cdebom/splus_morph

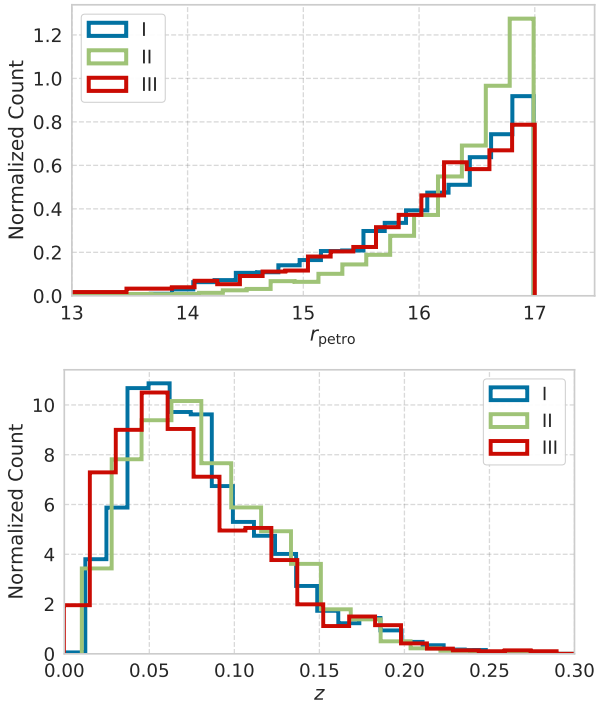

Figure 1. *Top:* Normalized histogram of the distribution of the r-petrosian magnitudes (r_{petro}) for the three sub-samples considered in our analysis (I, II and III). The majority of the galaxies lie in the faint-end of the distribution. *Bottom:* Distribution of spectroscopic redshift in the current sample (Molino et al. 2020)).

2 DATA

2.1 S-PLUS

S-PLUS is an optical survey using 12-bands (the so-called Javalambre magnitude system, described in Cenarro et al. 2019a) that includes 5 SDSS-like bands and 7 narrow-bands centered on important stellar features (the Balmer jump/[OII], Ca H+K, Hδ, G-band, Mg b triplet, Hα, and the Ca triplet). The survey's depth is r<20 AB mag for the narrow bands and r<21 AB mag for the broad bands. S-PLUS is performed with the T80-South Brazilian robotic telescope located at Cerro Tololo Interamerican Observatory, equipped with a 9.2k×9.2k e2v detector with 10 μm pixels, resulting in a field-of-view of 2 deg^2 with a plate scale of 0.55″ pixel^{-1}. The first public data release of S-PLUS (DR1) covers ~ 336 deg^2 over the Stripe-82.

We have used the full catalogue of the S-PLUS DR1 that comprises 3M sources including galaxies, quasars and stars (more details can be found in Nakazono et al, *submitted*). Specifically, we employed two quantities of that catalogue in order to define the galaxy sample: the magnitude in the Petrosian region in *r*-band (r_{petro}) and the probability of an object to be a galaxy ($prob_{gal}$). The interval criteria for these two quantities are:

$r_{petro} < 17$ AB mag and $prob_{gal} \geq 0.6$

Following these selection criteria, image stamps for the selected objects were created in the 12 S-PLUS filters for all the 170 fields in DR1. We kept the same standard stamp size for all images of 256×256 pixels[2]. This image size represents a good compromise between the size of the object and the stamp's dimension, to diminish the noise arising from the background in the fitting procedure and the inclusion of neighbouring galaxies. The stamps, in fits format, directly inputted in the pipeline. Thus, we avoid any loss of information due to format conversion or data compression. As shown in the top panel of Figure 1, the majority of the galaxies falls into the faint-end of the brightness regime, assuring that all the visible galaxy light fall within the image size. Moreover, the DNN algorithm used in this contribution requires the inputs to have the same size. Figure 2 presents an example of the 12 stamps for an E (top panels) and S (bottom panels) galaxies.

For every image, we also perform a cleaning process in which foreground stars and other objects are removed. We make use of GALCLEAN[3], which replaces bright sources with the noise distribution of the background. However, for the DNN method, we still use the original images stamps during training, validation and classification. As in some cases the masked image, resulting from the cleaning process, may contain artifacts (due to the masking procedure) and compromise the performance of the DL analysis. In fact, the DL algorithm may recognise the artefacts as an important element of image-recognition whether the features are quite large compared to the galaxy image, or a similar artefact (as a saturated masked star) is present in several images. Nevertheless, these masks are crucial for the morphometric processing (see Section 4).

2.2 Galaxy Zoo 1

GZ1 was a citizen-science project that ran from July 2007 until February 2009 and involved hundreds of thousands of volunteers to visually classify SDSS images in the GZ1 platform . It allowed not only the classification of nearly 900,000 objects (Lintott et al. 2008, 2010), but also the discovery of other classes of objects, as, for example, green peas (Cardamone et al. 2009; Lintott et al. 2008), and supported a number of follow-up studies, such as those on galaxy spins (Land et al. 2008; Slosar & White 2009) and mergers detection (Holincheck et al. 2016). In this paper, we use the wealth of data provided for galaxy classification by GZ1, to train a new galaxy S-E classification for S-PLUS objects. We selected only galaxies with known spectroscopy (from SDSS DR7), for which the so-called *debiased* classification (Bamford et al. 2009) from GZ1 is available (Lintott et al. 2010)[4].

In fact, a classification bias is present in GZ1 (Bamford et al. 2009; Lintott et al. 2010), due (i) to the sample selection (magnitude limits and the small volume at low redshift) and (ii) to signal-to-noise ratio and resolution effects. GZ1 provides four main classes: 'S', 'E', 'don't know' and 'merger'. The classification scheme assumes that galaxies that present spiral arms or are edge-on are classified as S while the remaining are considered E galaxies. Faint and small objects, though, tend to be classified as early-type galaxies, since spiral features are hard to be identified in such cases.

Bamford et al. (2009) developed a method to debias the classification for galaxies of known luminosities, sizes and distances, by assuming that their morphological fraction does not vary with the survey depth in bins of galaxy parameter space (i.e. bins of redshift,

[2] The image cutout tasks can be found in this GitHub repository: https://github.com/lucatelli/splus-tools.
[3] https://doi.org/10.5281/zenodo.4004571 (Ferreira et al. 2017; de Albernaz Ferreira & Ferrari 2018).
[4] Data obtained from https://data.galaxyzoo.org/, Table 2, for reference.

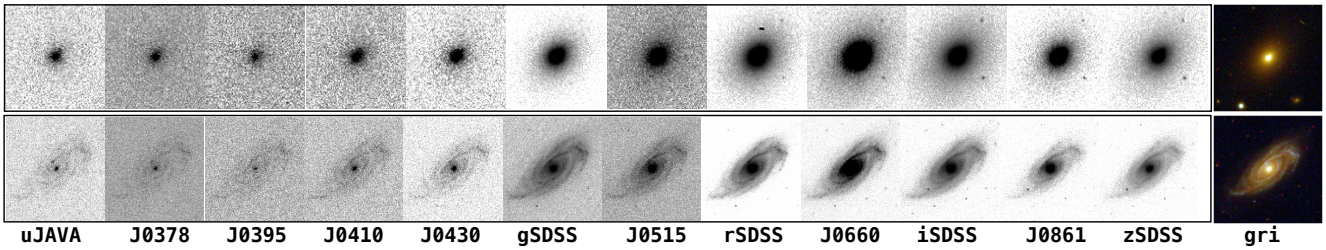

Figure 2. Example of image-stamps showing an E galaxy *(top panels)* and a S galaxy *(bottom panels)* in the 12 filters of S-PLUS. The last two panels show the *gri* colour images.

luminosity and size). To avoid problems due to the low volume at low redshift, the first redshift bin, for which the debiasing technique is applied, starts at $z \geq 0.03$. Unfortunately, the debiasing technique leads to the non-classification of several objects. It is important to note that the classification bias is not due to volunteers' involvement in the study, but to the limitation of the data.

The merger class, which comprises less than 1% of the classified galaxies and requires a detailed study to consider projection effects, will be studied in a separate paper (Mendes de Oliveira et al. in prep.). A class that was not considered in the GZ1 project is that of the lenticular (S0) galaxies which, in practice, fall in the S or E classification. Even for an expert, it is hard to disentangle a face-on S0 galaxy from an E galaxy or an edge-on S0 galaxy from and edge-on S. Bamford et al. (2009) found that the majority of the S0 galaxies fall into the E galaxy class, and they suggest that this class is referred to as early-type galaxies. In this work, we will follow this suggestion, leaving to a subsequent S-PLUS paper the challenge of finding bonafide S0 galaxies (Lucatelli et al. in prep.).

2.3 Deep Learning Sample Definitions

In this work, we use the debiased S and E GZ1 samples matched with S-PLUS DR1 as a *training and validation set* (sub-sample I); the GZ1 objects that, after the application of the debiasing technique, have no classification and matches S-PLUS DR1, constitute the *ambiguous set* (sub-sample II); and S-PLUS galaxies with no counterparts in the GZ1 sample are our *blind set* (sub-sample III). In Figure 1, we show the histogram of the distribution of r_{petro} and z_{spec} for each sub-sample. More details about these three sub-samples are given below and are also summarized in Table 1.

2.3.1 *Training and Validation Set - I*

This sub-sample comprises all objects classified by the GZ1 project as 'S' or 'E' in Stripe-82 (in total, 4232 objects). We use these objects to train, validate and test the deep learning network. The distribution in magnitudes of this galaxy sub-set is indicated by the blue line histogram of Figure 1 (top panel).

2.3.2 *Ambiguous Set - II*

Considering the debiasing technique (Bamford et al. 2009), we found $\sim$ 52% of the galaxies (4686 objects) in our S-PLUS DR1 sample classified as *ambiguous* in GZ1. It is worth noticing that in the distribution of the r band magnitude, as shown by the green line histogram in Figure 1, the galaxies are in average fainter than in the other two sub-sets (I and III). Consequently, it is harder to identify the presence of spiral arms, as pointed out by Bamford et al. (2009) and Lintott et al. (2010).

2.3.3 *Blind Set - III*

The third sub-sample (III) represents the data that does not have classification provided by GZ1. The final number of objects in this set represents $\sim$ 26% (3274 objects) of the total galaxy sample. We also refer to this sample as *unclassified*. Since this group is 'uncertain' (i.e. it has $\sim$ 40% probability of being a star), we made a visual cleaning on the image stamps. We also checked the quality flag `QF` from Morfometryka (Ferrari et al. 2015; see Section 4.1) in order to remove possible non-galaxy objects. In conclusion, only 14% have `QF` $\neq 0$, which might be caused by, for example, 'non-galaxy' objects, foreground stars close to the galaxy, or errors during the Sérsic fit (see Ferrari et al. (2015) for more details about `QF`). Such objects, as well as the objects identified as 'non-galaxy' during the visual cleaning, have been excluded from this sub-sample, rendering it low contaminated by outliers. Note that this sub-sample's redshift distribution is shifted toward lower redshifts with respect to the other two sub-samples (see Figure 1, lower panel). As explained in Section 2.2, only galaxies with $z \geq 0.03$ have been included in GZ1.

3 DEEP CONVOLUTIONAL NEURAL NETWORKS

3.1 Convolutional Neural Networks for Image Classification

Convolutional Neural Network (CNN) algorithms are a class of DNN techniques that makes use of a particular type of layers named convolutional layers. These layers were inspired in how animals visual cortex perceive patterns (Hubel & Wiesel 1962; LeCun et al. 2015). They consist of kernels that are convolved with the data as they flow through the DL model. The DNNs for pattern recognition in images are commonly based on several stacked convolutional layers among with dimensionality reduction layers (or pooling layers) and regularization layers (e.g., dropouts or batch normalizations, see Goodfellow et al. 2016; Chollet 2018). The trained kernels act as filters specialized in the identification of a specific pattern in the data. Those layers are later connected to traditional fully connected neural network layers that take into account the particular features from the previous layers and outputs the predicted class based on a softmax function (Goodfellow et al. 2016). This function returns a vector with the probabilities of the respective potential classes.

In their notorious paper, LeCun et al. (1998) introduced the first widely recognized successful application of these convolutional layers for image identification of handwritten digits. Since

Table 1. Sample Description. In our sample the data are separated into three groups as indicated below.

Name	Number of objects	Description
I	4232	S and E galaxies matched with GZ1 in S-PLUS DR1 after magnitude cut
II	4686	Ambiguous galaxies matched with GZ1 in S-PLUS DR1
III	3274	Remaining unclassified galaxies in S-PLUS DR1

that, CNNs have become the primary technique on this field, and its several based architectures won the main computer vision community competitions (see, e.g. Russakovsky et al. 2015; Krizhevsky et al. 2012), making use of several different CNN based models such as VGG (Simonyan & Zisserman 2014), ResNet (He et al. 2016) and Inception models (Szegedy et al. 2015, 2016).

Many patterns of interest in astrophysics can be visually assessed. This spurred the use of CNNs in the field, as the aforementioned examples of pioneering galaxy morphological classification in Section 1. One of their major successful visual pattern recognition applications in astrophysical data was the search of Strong Lensing systems. This task has been widely explored both in simulated and real data (see, e.g. Bom et al. 2017; Jacobs et al. 2017; Lanusse et al. 2018a; Petrillo et al. 2019a,b; Cai et al. 2020) and they also have their own computer vision challenges (Metcalf et al. 2019; Metcalf 2021), which were both won by CNN-based architectures. It is worth noticing that the model with the best performance in the latest Strong Lensing Challenge its a variation of a family of CNN models known as EfficientNet (Tan & Le 2019) that represents the state-of-the-art in one of the most acknowledgeable datasets in computer vision: the ImageNet (Deng et al. 2009). We make use of this kind of model in this contribution as our base model for addressing the morphological classification task.

3.2 EfficientNet Models

EfficientNets are a family CNN based models that were scaled and optimized considering a computational resource constrain and accuracy. In its original paper Tan & Le (2019) proposes to start with a model similar to a mobile CNN (Howard et al. 2017). A multi-objective neural architecture search (Tan et al. 2019) is performed into this initial model to optimize both accuracy and Floating-point Operations Per Second (hereafter FLOPs). The resulting model is the base model known as $B0$. This approach, known as Auto Machine Learning (henceforth AutoML), tests several Neural Network hyperparameters combinations to optimize the Machine Learning model, and it is fully described in the previous references. After the $B0$ model is defined, Tan & Le (2019) proposed a set of scaling relations to define the width of the layers, i.e. how many kernel units in a layer, the depth, the convolutional blocks and layers and also the resolution of input images. Therefore, constraining the space of DNN hyperparameters to be explored in the optimization processes. The intuition for these quantities is that if deeper networks are more prone to learn complex features, on the other hand, they are also more likely to find vanishing gradients, while wider networks and high-resolution inputs are expected to learn fine-grained features (Zagoruyko & Komodakis 2016; Howard et al. 2017). In this case, the trade-off is that if one defines an excessively wide network, it becomes harder to learn the complex features. It is worth mentioning that deeper networks are also expected to saturate in accuracy (He et al. 2016), thus going deeper might result in unnecessary computational time and other convergence issues.

These scaling relations can be defined as follows:

$$\begin{aligned} &\text{depth: } d = \alpha^{\phi} \\ &\text{width: } w = \beta^{\phi} \\ &\text{resolution: } r = \gamma^{\phi}. \end{aligned} \tag{1}$$

ϕ is an integer named compound coefficient. The coefficients α, β, and γ are optimized by a small grid search in the base model, i.e. with fixed $\phi = 1$. The number of FLOPS scales with $d \cdot w^2 \cdot r^2$ or, in terms of Equation 1, with $(\alpha \cdot \beta^2 \cdot \gamma^2)^{\phi}$. Thus, to constrain the FLOPs to 2^{ϕ}, the coefficients α, β, and γ are subject to the following constraints:

$$\begin{aligned} &\alpha \cdot \beta^2 \cdot \gamma^2 \approx 2 \\ &\alpha \geq 1, \beta \geq 1, \gamma \geq 1, \end{aligned} \tag{2}$$

Under this procedure, one may define a family of EfficientNets from the base model $B0$ to any BN where $\phi = N$. It is worth noticing that scaling up an already optimised CNN is a process orders of magnitude less computationally intensive than a fully neural architecture search. This might become prohibitive for many available computer facilities if one has a fixed computation time budget since the number of parameters is of the order of millions or dozen of millions.

For the Morphological Assessment of galaxies, we made use of the EfficientNet $B2$ model architecture proposed in the original Tan & Le (2019) paper. This network architecture was applied to identification of Strong Lensing (Metcalf 2021) winning the II Strong Lensing Classification Challenge. The $B2$ was compared with other EfficientNet models ($B0 - B7$) using our baseline input set of g, r, and i bands for morphological classification. The results were similar in terms of accuracy except for the networks with higher numbers of parameters which are the ones more prone to overfit. The $B2$ model was adapted for our problem: the top layer was modified to output the probability of being a S or an E galaxy. Another significant change was the use of recent state-of-the-art adaptive learning rate optimiser named Rectified Adam (RADAM Liu et al. 2019). The authors of RADAM have shown empirically that the rectification term applied in the conventional ADAM (Kingma & Ba 2014) optimiser leads to a faster, more stable optimisation which is less sensitive to the choice of hyperparameters such as learning rates. The EfficientNet models are among the highest-ranked in terms of performance for image classification tasks, given an informative (in terms of variety) and sufficiently large structured image dataset as presented by Tan & Le (2019), outperforming many of the aforementioned computer vision data challenge winners.

4 GALAXY MORPHOMETRY

Alongside the CNN approach (Section 3), an additional analysis has been performed in this work to recover the morphometric parameters for all three sub-samples and compare their distribution.

Such comparison is a sanity check of the CNN classification, since we are able to evaluate whether the same behaviour of the parameters, recovered using Morfometryka (hereafter MFMTK, see Ferrari et al. 2015) in the training and validation set, is present in the *ambiguous* and *blind* sample. Moreover, galaxies of different morphologies present different values of morphometric parameters (Conselice 2014) such as concentration and entropy. Thus, calculating the distribution of such parameters for the E and S galaxies classified by the CNN can link the galaxy morphology from computer vision to its structure and physical properties from morphometry. MFMTK and the main morphometric parameters used for this analysis are described in the following sections, while results of this analysis are presented in 6.4.

4.1 Morfometryka

The morphometric processing is performed using Morfometryka (Ferrari et al. 2015), and it includes photometric (geometric and Sérsic parameters) and morphometric measurements, e.g. CASGM-$\sigma_\psi H$ system. All measurements computed by MFMTK are done in an automated way, which only needs the image and its PSF as inputs. For the analysis and comparison of morphometric parameters, we select the concentration and entropy measurements, since they are more stable in relation to image resolution and signal-to-noise (Ferrari et al. 2015; de Albernaz Ferreira & Ferrari 2018) . A more general study of all morphometric and photometric parameters recovered with MFMTK is left to another dedicated work, where a more detailed analysis will be conduced using Machine Learning techniques (Lucatelli et. al, in prep).

4.2 Concentration and Entropy

Concentration (C) (Kent 1985; Bershady et al. 2000) is widely used to quantify how the brightness of a galaxy is distributed within it. C is defined as the ratio between two percentile radii of the galaxy. One example is the C index defined considering the radii that contains 80% and 20% of the total luminosity; in that case, $C \propto R_{80}/R_{20}$. In MFMTK, there are different C definitions:

$$C_1 = \log_{10}\left(\frac{R_{80}}{R_{20}}\right), \quad C_2 = \log_{10}\left(\frac{R_{90}}{R_{50}}\right). \tag{3}$$

Generally, E galaxies, compact galaxies and classical bulges have higher concentration values than S, disk-like galaxies or pseudo-bulges.

Complementary to C, the entropy (H) of a galaxy image (Ferrari et al. 2015) quantifies how the light is distributed in the image. The entropy adopted by MFMTK is based on Shannon entropy,

$$H = -\frac{1}{H_{\max}} \sum_{k}^{K} p(I_k) \log\left[p(I_k)\right], \quad H_{\max} = \log K. \tag{4}$$

where I_k is the intensity value of I at position k and $p(I_k)$ is its probability of occurrence. $H_{\max}$ is the maximum value of entropy, which means that all pixels have the same probability : $p(I_k) = 1/K$ with K being the number of bins. An image with a homogeneous distribution of pixel values will have higher entropy than an unequal distribution (Bishop 2007). In this sense, E galaxies may have a lower H in relation to S galaxies.

Table 2. Short description of the models used.

Name	Description
A	g, r, i bands. No pre-training
B	g, r, i bands, Model pre-trained with ImageNet
C	5 broad bands, g, r, i, u, z. No pre-training
D	5 broad bands and 3 narrow bands, F515, F660, F861. No pre-training
E	12 bands: 5 broad bands and 7 narrow bands. No pre-training

5 TRAINING AND VALIDATION

5.1 Preprocessing

The images were normalized, this is a useful practice for neural network training convergence (Goodfellow et al. 2016). A simple image contrast adjustment was performed saturating the bottom 1% and the top 1% of all pixel values. We randomly inspect the images to check for quality or issues. In Section 7.2 we present some panels containing image examples. In the unlabeled sample, we also had to define a slightly different saturation level as this sample has more galaxies in the faint end and some close to saturated stars. For training purposes, we made use of data augmentation techniques. This procedure is known to increase DNN performance (see, e.g., Chollet 2018). The augmented sample was not used in the validation samples or any network quality metrics, only to enhance the training. To define the augmented sample, we use 180 degree rotation, horizontal flip and vertical flip.

5.2 Imbalanced data treatment

The train/validation dataset is obtained by cross-matching the S-PLUS catalogue with the debiased morphological catalogue of GZ1, as explained in Section 2.2. It contains 71% of S galaxies and 29% Es, reflecting the early-type to S ratio at z $\simeq$ 0.03 of the GZ1 datasets. In fact, such ratio is taken as a baseline estimate in the process of debiasing, which assumes that this fraction does not evolve with redshift for bins of fixed luminosity and size (see Appendix A of Bamford et al. 2009 for a detailed explanation of the debiasing technique).

We present the distribution of both classes in Figure 3. Due to the data imbalance between the two classes we apply a standard procedure[5] to weight each class. We define the weights of a certain class α as:

$$w_\alpha = \frac{N}{mN_\alpha}, \tag{5}$$

where N is the number of objects in the training set, N_α is the number of objects in the class α and m is the number of classes. The weights are applied in the objective function, so each class has the same impact in the optimization process. Therefore, the procedure prevents the model to bias towards the class with more samples and loose generalization capacity. This is particularly important in problems where one class has orders of magnitude more samples than the other (Sun et al. 2009).

[5] see, e.g., https://www.tensorflow.org/tutorials/structured_data/imbalanced_data

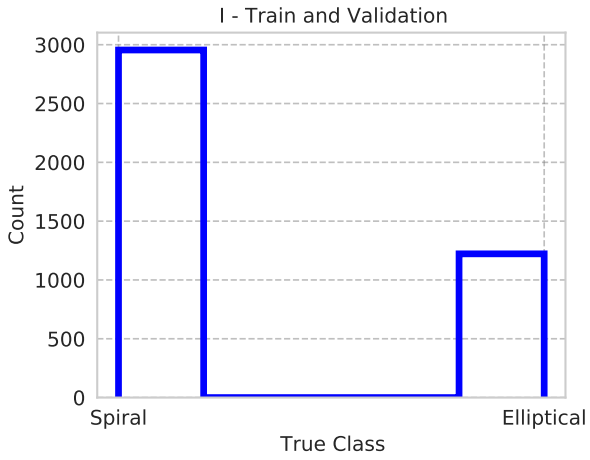

Figure 3. Distribution of galaxy labels in the train/validation sample: i.e. number counts of galaxies classified as E or S in the unbiased GZ1 data release, present in the S-PLUS DR1 data release, see Section 2.2.

5.3 Training

We used the dataset I in Table 1 described in the previous sections, with the true GZ1 for training and validation purposes. We made use of a standard backpropagation procedure to minimize a cost function, also named as *loss*. This function is defined to be a cross-entropy function:

$$H(p,q) = -\sum_{x\in\mathcal{X}} p(x)\ \log q(x), \tag{6}$$

where $p(x)$ is the galaxy labelled probability of an object pertaining to a certain class (either 0 or 1 in our case) and q(x) is the probability predicted by our DL method. We split the dataset in 5 folds to perform a cross-validation procedure (Moreno-Torres et al. 2012). Thus we define 5 different training and validations sets containing 80% and 20% of the dataset I, respectively. We define the first fold as validation and the other 4 as the training set for the first set. After the training procedure, we redefined the validation set as the second fold and the others as training. It is worth mentioning that the training subset for each fold is the only one used to update the network's weights in the backpropagation algorithm (Ruder 2016). To decide which is the best network set of weights, we perform 50 epochs and choose the weights defined in the epoch with lower validation loss. The latter would be the weights, to be given to the network, that better generalize the results for a given validation set, unknown to the network training procedure. The cross-validation method defines one network configuration per training/validation split, which makes possible to evaluate how robust is the training for different sets. Additionally, this method guarantees that each object will be used at least once in the test set.

Using the architecture defined in Section 3.2, we set up different models varying the kind of input or the use of preset weights initialization. The models are described in Table 2. The model A makes use of three broad bands g, r and i in a traditional 3 channel scheme for image classification in data science problems (Deng et al. 2009) using a uninformative weights initialization (Glorot & Bengio 2010). To evaluate the effect of pre-trained weights initialization, we define model B using the same 3 broad bands. This model also starts with weights derived from pre-training from ImageNet dataset. This idea is known as transfer learning (Yosinski et al. 2014). It consists of using a given model (that is, an architecture and its weights) that learned in a given task/data domain, in our case classifying the ImageNet classes, as a base model for another task/data domain. This method relies on the hypothesis that a sufficiently large and well fitted DL model is effective in learning features and some of those features can be shared among tasks like different sets of image classification problems. We let all the weights free to be optimized in our training, which means that we only used the pre-trained weights to initialize the network. The subsequent models do not use the pre-trained initialization since they are defined in a different number of channels than the original ImageNet. Model C makes use of all 5 available broad bands g, r, i, u, and z. Model D is set to use the aforementioned broad bands and also 3 narrow bands with higher signal-to-noise ratio, namely $F515$, $F660$ and $F861$. These bands can retain information of important stellar features, such as $H\alpha$, Mgb triplet, and Ca triplet. Yet those emission lines fall into the corresponding filter only till a certain redshift (for example, the $H\alpha$ line falls into the $F660$ filter only until $z \simeq 0.015$). Given the redshift distribution of the galaxies in this sample ($z_{max} \simeq 0.3$, $z_{peak} \simeq 0.05$); see the lower panel of Figure 1), this is not the case for the majority of the targets, and the differential factor for the $F515$, $F660$ and $F861$ images is the higher S/N among the narrow band images (see Figure 2). Finally, model E makes use of all available broad and narrow bands from S-PLUS (a total of 12).

The training plots are presented in Figure 4. The left panel presents the optimisation in the training dataset, and the right panel presents the training performance in the validation dataset. All the models have a satisfactory optimisation in terms of training loss. However, the model with pre-trained ImageNet weights did perform better in terms of median loss in all folds. The baseline model with 3 bands presented a high instability in the training process and did not converge to a minimum in all the folds; thus, it presents a high variance for training loss in the folds. On the other hand, the models with 5 and 8 bands had a more stable convergence and performed similarly. It is worth noticing that, regarding the validation loss, none of the models present strong overfitting considering their variability in the folds. However, by looking into individual folds, we observed that the models with 5 or more bands tend to overfit after ≈ 40 epochs. For the following analysis, we use the models at the epoch with lower loss in the validation sample.

It is also worth noticing that all considered configurations, except the pre-trained with ImageNet, optimised the loss function in early epochs. However, the validation loss needed several epochs more to reach a comparable low value indicating that the DNN learned how to generalise for a dataset different from the one used in training (e.g. the validation dataset).

6 RESULTS

6.1 Model Performance

The model performance is evaluated only in the validation sets, i.e. the set that was not used to optimize the DNN weights during the training. The uncertainty in each metric is derived by the k-folding procedure described in the previous section. We consider as metrics the purity (or precision), completeness (or recall), and false alarm rate (or false positive rate). The precision for the sample of galaxies of a class α is defined as:

$$\text{precision} = \frac{|\{\text{Galaxies in } \alpha\} \cap \{\text{Galaxies classified as } \alpha\}|}{|\{\text{Galaxies classified as } \alpha\}|}. \tag{7}$$

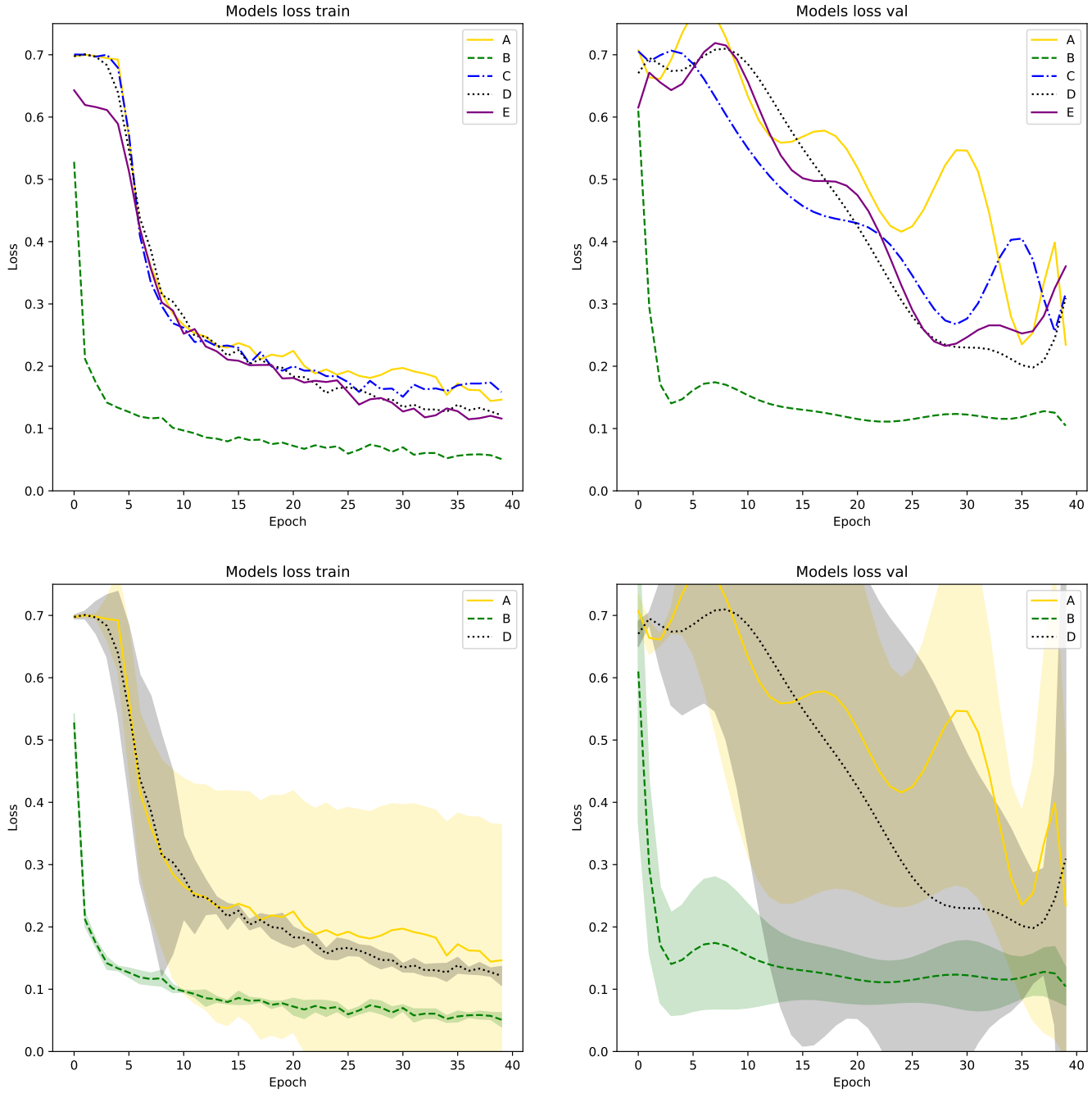

Figure 4. The objective function results for: A, C, D and E are the results for the 3-,5-,8-, and 12-band models, respectively, all without ImageNet weights. Model B is a 3-band model used ImageNet pre-trained initialization weights. The shaded regions represents the standard deviation in the folds due to cross-validation procedure.

The recall can be defined as:

$$\text{recall} = \frac{|\{\text{Galaxies in } \alpha\} \cap \{\text{Galaxies classified as } \alpha\}|}{|\{\text{Galaxies in } \alpha\}|}. \quad (8)$$

The false alarm rate is:

$$\text{false alarm} = \frac{|\{\text{Galaxies not in } \alpha\} \cap \{\text{Galaxies classified as } \alpha\}|}{|\{\text{Galaxies not in } \alpha\}|}. \quad (9)$$

As the DNN outputs a number representing each class's score (E or S), to obtain a precision and recall, it is necessary to define a threshold t. If a given probability of a class in our validation dataset is above the threshold (i.e., $p > t$), we consider the object as part of this class. To define an optimized threshold and also to assess the performance, we plot the precision and recall and the Receiver Operating Characteristic (ROC, i.e. recall and false alarm rate) curves for any threshold in the range [0, 1]. The Area Under the Curve of the ROC curve (AUC) is an intuitive measurement of classification performance: a perfect classifier would have AUC = 1. In contrast, a random choice in a balanced dataset would have AUC = 0.5. The

perfect classifier is the one that approaches the point (0, 1), i.e. 0% false positives for 100% completeness.

It is worth noticing that all models presented here have a high performance in terms of AUC, with median AUC > 0.98. In Figures 5 and 6 we present the ROC for models A to E. For E galaxies, we noticed that all models, except the one with 12 bands, have similar performance, close to AUC = 0.99 with ≈ 0.01 sigma. The model pre-trained with ImageNet is more stable in terms of AUC, and this model is the one that gets closer to the perfect point (0, 1). The ROC in the S case favours the aforementioned pre-trained model, but also the 5- and 8-band models have a similar performance. We see that the model with 3 bands only has a higher error in AUC and tends to deviate from the (0, 1) point if compared to the others.

The figures of precision and recall present a more clear picture of the models. We still see that the model with 3 bands only with no pre-training performs worst in the median curve and has a high average precision error compared to others. The 12 band model presents no gain compared to 5 or 8 bands. The models with 5 broad bands and 8 bands have similar results. However, the first has a very stable result on average precision for S galaxies. The most notable difference, except for the aforementioned model, is that the model with 3 bands only seems to be more sensible to the trials between test and validation for E galaxies. The 5-band model also gets closer to the perfect-classifier point (0, 1) than the 8-broadband model for E galaxies. However, the results show that 8- and 5-band differences are marginal. We present a more detailed picture considering the deviations in the five K-folds for the pre-trained model, the result for our base model with 3 bands only, and the 8-band model in Figure 6.

Considering these results, we define the best threshold to be the one closest to the point (0, 1) in AUC. We present our results for the confusion matrix in Figure 7 using the pre-trained network. This model consistently presented a high performance with high stability in both ROC and precision-recall curves and required fewer inputs than the other similar model with 8- or 5-bands. The confusion matrix represents the overall performance of true positives, true negatives, false positives and false negatives. Considering all the K-folds, we misclassify 15 ± 2 objects in our validation sample, representing less than 2% (and therefore accuracy of 98%) for any object with $r < 17$ AB mag, in all redshift ranges considered.

6.2 Application to ambiguous and Galaxy Zoo unlabelled dataset

We apply our best model, EfficientNetB2-like architecture using pre-trained weights from ImageNet in three bands to the other two samples. In Figure 8, we present a histogram that gives the score distributions for the three datasets: training and validation, ambiguous, and unclassified/blind samples. We emphasize that the distributions are qualitatively similar; the model presents high confidence in the non E probability end. The ambiguous sample presents a more smooth distribution which might be an indicator that this sample presents a major challenge to the DNN.

6.3 Testing the S-PLUS E-S classification: comparison with other morphological classifications

Figure 9 shows the comparison between results from this work with other morphological classification of Stripe-82, based on DL (Domínguez Sánchez et al. 2018; left column) and visual morphological classification (Nair & Abraham 2010; right column). The first row shows the results for the training-validation set, the second row, those for the ambiguous set, and the last row, those for the blind set. In the left column, the histogram showing the distribution of the galaxies classified as E has a peak at T-Type = -2.5 and generally the distribution falls below T-Type < 0, for the three cases. Galaxies classified as S have a broader distribution, which peaks around T-Type = 4.5 for the training-validation and blind sample. Yet, some galaxies classified as S have a T-Type lower or around zero, due to the difficulties of discriminating the presence of spiral arms in faint and higher-redshift galaxies, as discussed in Section 2.2. This effect is stronger in the ambiguous class, exemplifying how this group of galaxies, if taken into consideration, would lead to an incorrect S-to-E galaxy ratio in the local Universe, and were therefore excluded during the debiasing process (Bamford et al. 2009). The right column of Figure 9 shows the histograms comparing the distributions of the E-S classification of this paper with respect to the T-Type visual classification from Nair & Abraham (2010), for the training-validation set, the blind, and the ambiguous sets. Unfortunately, when matching Nair & Abraham (2010) and the catalogue presented in this work, the sub-sample of objects in common is not large (≥ 100 objects). Even so, there is a clear agreement between the two classifications, with the only exception of T-Type = 0 (i.e., the S0 class), which is hard to classify since it is not explicitly considered in the classification procedure of this paper and it will be implemented in Lucatelli et al. (in prep).

6.4 Testing the S-PLUS E-S classification: morphological parameters of the newly classified galaxies

In order to evaluate how the morphometric features would be distributed in the sample, we obtained measurements of C and H. We compare these features to what we would expect for S and E galaxies, given what is already known in the literature. The determinations of these quantities for the sub-samples in Table 1 are compared in Figure 10. This Figure shows the C_2-H morphometric diagrams for the three sub-samples (I,II and III), and the plots are colour coded according to the galaxy classification. All left plots refer to measurements only in the r-band and all plots on the right are made taking the mean of C and H in different filters. The top of Figure 10 indicates the distribution of C and H for the training and validation samples, while the middle and bottom of Figure 10 refers to the same analysis but for sub-samples II and III, respectively. In these plots, the E and S classifications are the results of this work.

We note that, given that the E-S classification of this paper is trained using GZ1, i.e. visual classification based on the shapes of the objects (with or without spiral arms) and the morphometric parameters also measure the monochromatic light distribution, this plot turns into a sanity check. The two methods, even if based in different techniques (classifications done by humans vs machines) recover the form of the objects, without taking into consideration the colour or stellar population of the galaxy.

The sub-sample measurements show a clear distinction between classes E and S, i.e., the centres of each contour lines are well separated. On the other hand, when looking to the ambiguous sub-sample, in the middle of Figure 10, the centres of the two distributions are not well separated. This reflects the fact that these objects are classified as uncertain, as it is clearly seen in the relation between C and H. Finally, for sub-sample III, at the bottom of Figure 10, the centre of E and S distributions are better separated in relation to the sub-sample II, nevertheless, with a larger scatter than the classification from GZ1 (sub-set I at the top).

Subsequently, when considering the same comparisons but us-

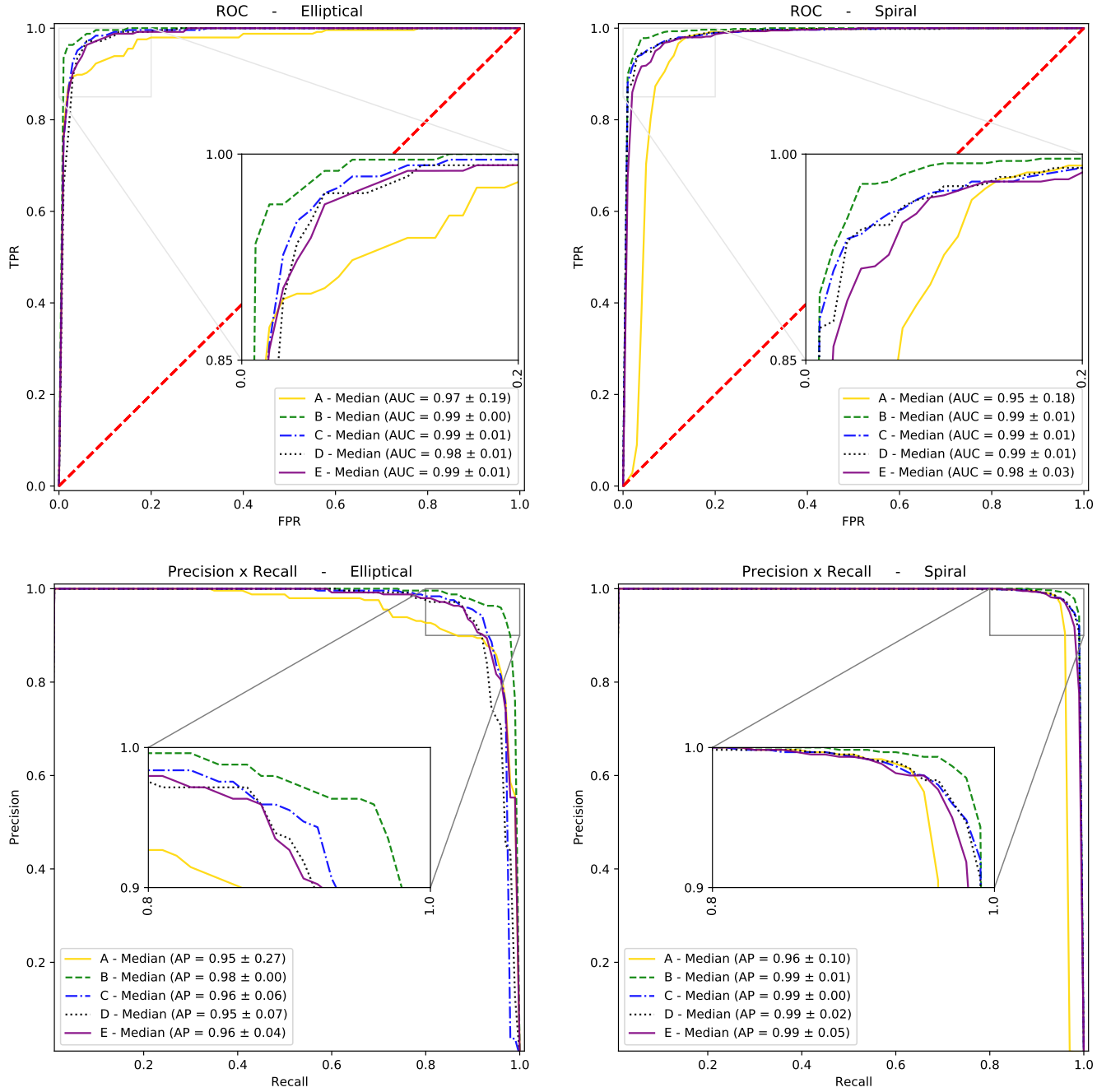

Figure 5. Results for A, C, D and E for the 3-, 5-, 8- and 12-band models, respectively. Model B used pre-trained ImageNet weights initialization with 3 bands.

ing the mean of C_2 and H in different filters (instead of using the r-band), we have a reduced scatter in the data. Still, the discrimination between 'E' and 'S' in sub-sample II is worst than for the others. The general conclusion is that the shape of the $C_2 - H$ morphometric diagrams are similar to what is already shown in the literature (Ferrari et al. 2015; Conselice 2014) and when we use the classification of the deep-learning approach adopted here, validating the results obtained in this work.

Finally, the left and central panels of Figure 12 show the $(g-r)$ and $(u-z)$ normalized colour distributions of the galaxies, colour coded according to the galaxy classification, for the three sub-samples (I, II and III). The two galaxy populations, E and S, present the expected colour bimodality, with classified E's being redder than S's. The third column shows the distribution of the bayesian spectral type (Tb) parameters, as obtained by Molino et al. (2020). Briefly speaking, to derive a photometric spectral measure (photo-z), from the galaxies' SED, it is necessary to fit, together with the redshift value, the most probable spectral type of the galaxy. The redshift is in fact determined from the shift of the observed SED with respect to galaxy templates used in the fitting routine. In this case, the results are obtained using BPZ (Benítez 2011) and are presented in Molino et al. (2020). The distribution of the Tb parameter shows that when the whole galaxy SED is taken into account, the colour bimodality of E-S galaxies is not so clear anymore, and the

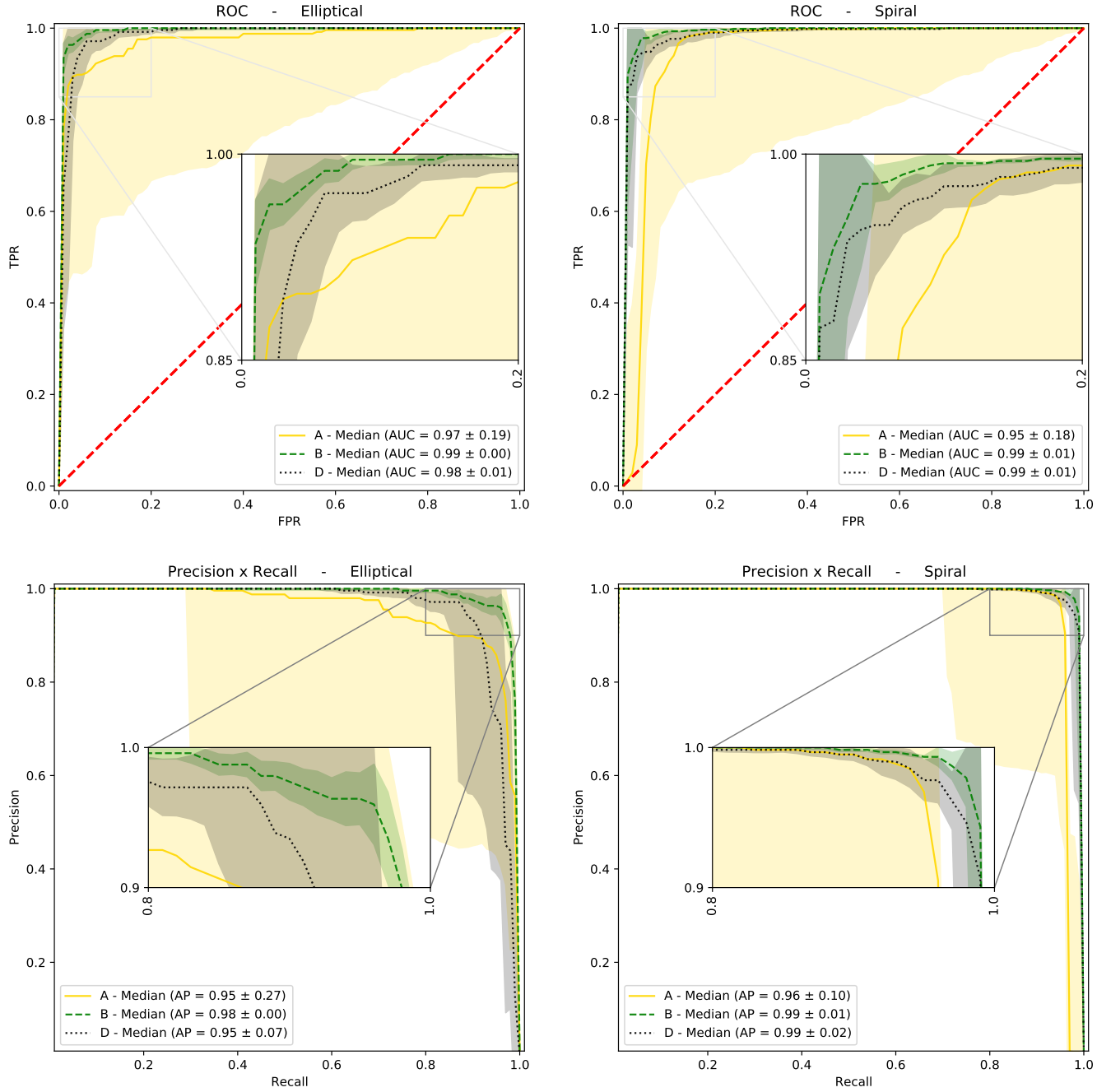

Figure 6. Results for A and D with the 3-, 8-band models, respectively. Model B used pre-trained ImageNet weights initialization with 3 bands. The shaded regions represents the standard deviation in the folds.

complexity of the relation between galaxy morphology and the stellar population is brought to light: quenching effects, as well as the influence of star formation bursts become detectable, using a full SED fitting or some specific narrow bands. This plot also reveals the potential of S-PLUS survey in studying galaxy evolution and formation.

7 DISCUSSION AND CONCLUDING REMARKS

7.1 Summary

In this paper, we use the state-of-the-art of DL methods for image classification and present a model for predicting astrophysical features of nearby galaxies in Stripe-82, observed within S-PLUS. Specifically, we recover their morphology, assigning each object a probability of being a S or an E galaxy, using artificial intelligence. We also evaluate the use of 12 bands presented in S-PLUS. Thus, we use different combinations of filters (broad and narrow), to check the effect of the inclusion of narrow bands in the analysis.

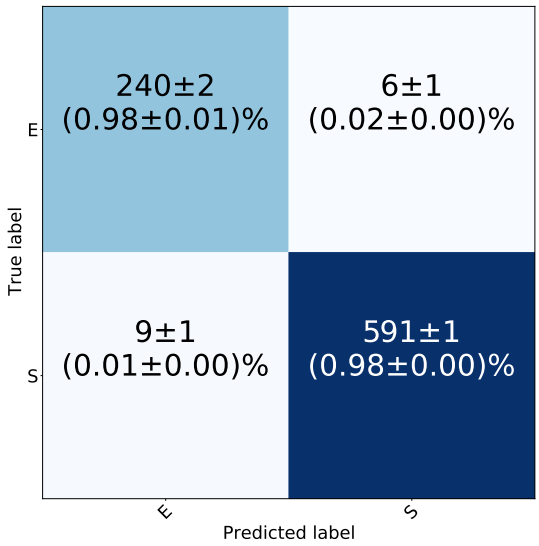

Figure 7. Confusion Matrix for the best model.

In fact, morphological classification using DL algorithms has been already implemented in several works (Domínguez Sánchez et al. 2018; Barchi et al. 2020; Tuccillo et al. 2016; Khalifa et al. 2018; Dieleman et al. 2015; Zhu et al. 2019; Dai & Tong 2018; Gupta et al. 2020; Vega-Ferrero et al. 2020). In this work, we investigate the gain/loss of adding narrow-band images to perform the classification. We also evaluate the use of weights extensively trained in other reference computer vision dataset to initialize the DNN. We deliver a new catalogue of galaxies morphologies, including a classification for galaxies considered ambiguous or unclassified in GZ1.

7.2 A New catalogue of Galaxy Morphology

The final catalogue we developed can be divided into three samples. The first was used as training and validation and it was already classified in GZ1 catalogues. Therefore, this sample acts as a quality control sample. This sample was crucial to develop working and high performance DNN models in S-PLUS. The model created from this set will pave the path towards the morphological classification in the whole S-PLUS footprint.

The second sample contains the galaxies considered ambiguous in GZ1. Our assessment using independent features to analyze the data suggests that these objects are indeed ambiguous in the parameter space of the morphological features used (C and H). However, we do see some degree of difference in the E and S groups classified by the current DL method. It is worth noticing that this group has more objects in the faint end than the control group.

The last group contains the objects that are not presented in GZ1 catalogue. Thus, we present a new classification for these objects using S-PLUS data with competitive quality to the human/machine performance used in GZ1.

The three groups together contain all the S-PLUS DR1 galaxies in Stripe-82 with r < 17, see Section 2 for more details.

In Figure 13 we present a visual assessment of randomly chosen galaxies in the full catalog in a certain confidence interval. It is clear that somehow we are biased toward the objects that have a higher number in the sample, i.e. as galaxies in top row: the images are quite shallow, nevertheless the deep learning algorithm is doing a great job in classifying as S's or E's. Then, we have more obvious cases, with larger and more clearly visible (at a human eye) spiral arms. Yet, since these types of galaxies are less present in the training sample, they get slightly lower values of probability (0.9). When the probability gets lower than 0.7, some cases of confusion are present. Yet, as possible to see in Figure 8, the number of cases with a prediction lower than 0.7 is scarce (in the case of the E galaxies, around 3 galaxies per bin of probability). The catalogue

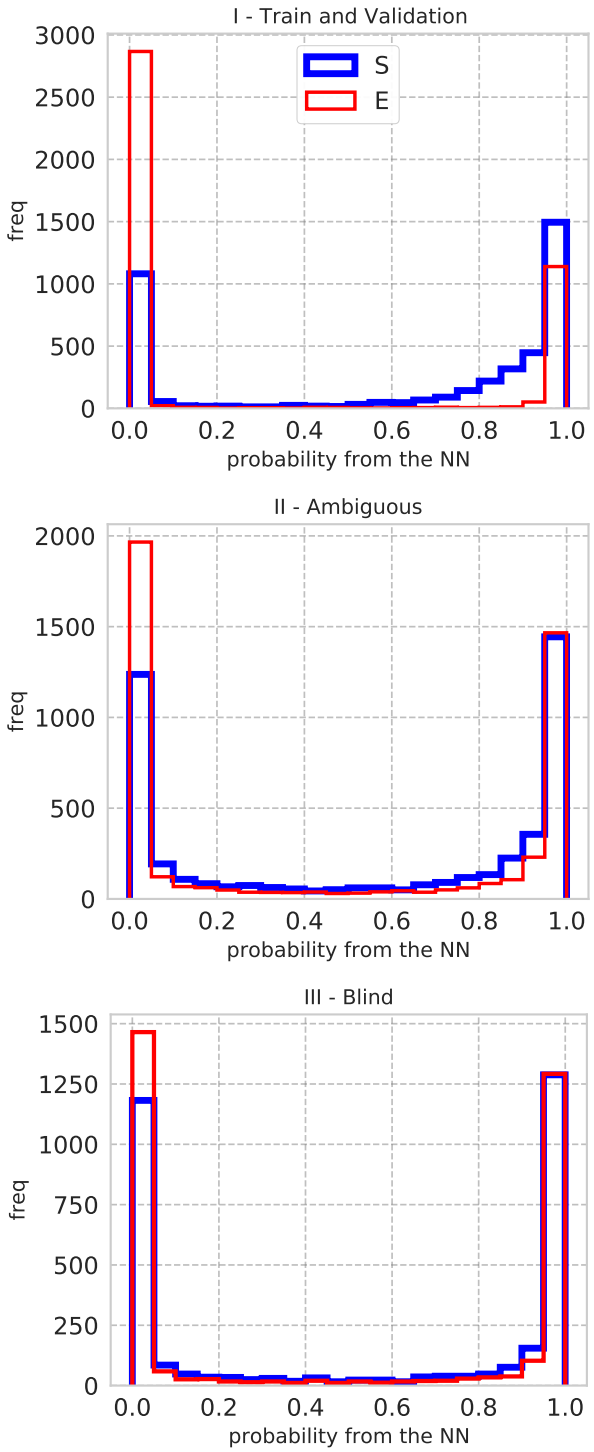

Figure 8. Distribution of probabilities (scores) for galaxies to be E or S provided by the Neural Network. From top to bottom, these are for the subsamples I, II and III, respectively.

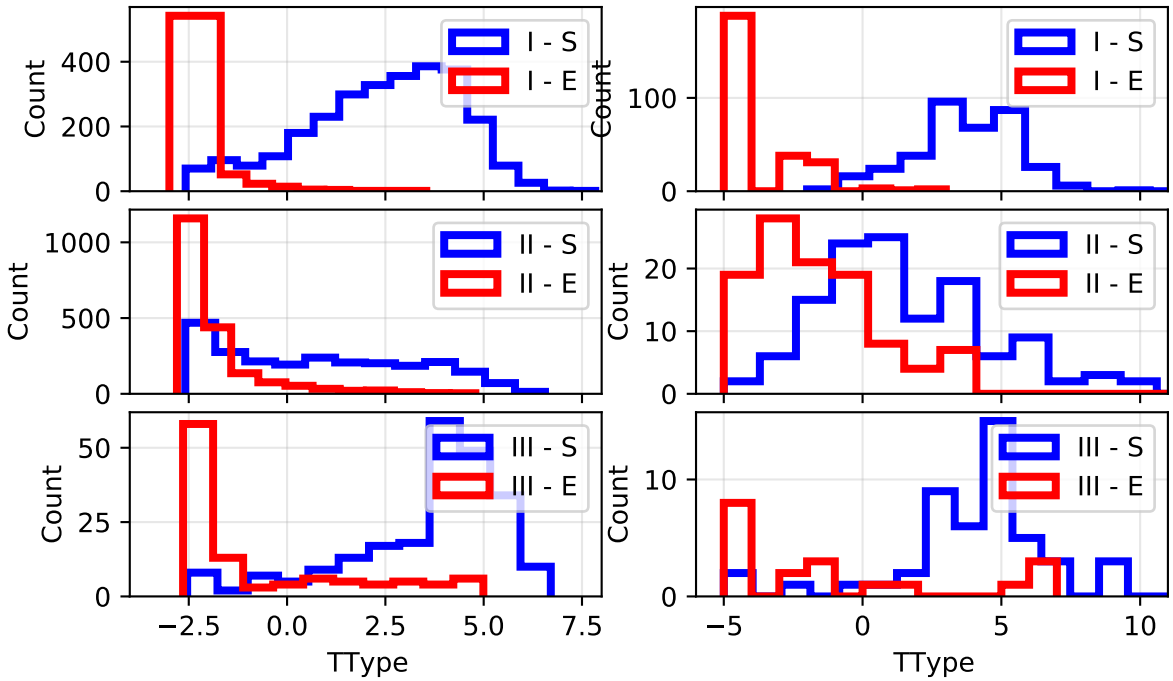

Figure 9. *Left:* Histograms comparing the distribution of the E-S classification of this paper with respect to the T-Type morphological classification from Domínguez Sánchez et al. (2018), for the training-validation set *(top)*, the ambiguous set *(center)* and the blind set *(bottom)*. *Right:* Histograms comparing the distribution of the E-S classification of this paper with respect to the T-Type visual classification from Nair & Abraham (2010), for the training-validation set *(top)*, the ambiguous set *(center)* and the blind set *(bottom)*. In general, S0s have $-3 \leq TType \simeq 0$.

released within this contribution contains the probability of each class and also our classification using the same threshold imposed in the confusion matrix described in Section 6.1.

7.3 The effect of using narrow bands

We compared 5 different models of DL: using 3 broad bands (with and without pre-training), 5 broad bands, 8 bands (5 broad bands and 3 narrow bands) and 12 bands. Note that this is the first time that automated multi-band galaxy classification is applied to more than 4 bands (Vega-Ferrero et al. 2020). Looking at Figure 6, it is possible to see that the best model is the one with 3 bands, pre-trained with the ImageNet, highlighting the importance of pre-training in this type of analysis (note, however, that for the moment pre-training is possible only for 3 bands as the ImageNet images contain three channels). In fact, when comparing the remaining four cases, with no pre-training, it is clear that the 3-band case has the worst performance: as mentioned earlier, it was the only one that did not optimize the training loss in all the folds. Interestingly, the 5- and 8-band models have the highest precision for recall (among the models with no pre-training), suggesting that using all the 12 bands, including some low S/N bluer narrow bands, might increase the confusion in the classification procedure, considering a DNN architecture with the same complexity. Not surprisingly, in the 8-bands model, the three narrow bands used are F515, F660 and F861, which have higher S/N. These findings suggest that this DL method can be efficiently applied to novel broad band surveys, such as LSST, with no much gain to the use of more bands in the current range of magnitudes and redshifts.

Another possibility would be to incorporate the current models in a Neural ordinary differential equations (NODE) approach as in Gupta et al. (2020). In fact, NODE is an efficient way to train a DNN that does not require large data set for training and we may find a gain using more bands, when implementing them in the pre-training.

7.4 Deep Learning performance and the relevance of traditional machine learning algorithms

Deep Learning exceeds human performance in several computer vision problems, including classification of astronomical sources (see, e.g. Metcalf et al. 2019; Metcalf 2021; Russakovsky et al. 2015). In particular, the validation set, not used for training the network weights, reached an accuracy of $\sim 98 \pm 1\%$, which leaves little room for improvement or any measurable bias towards magnitude or redshifts in the current sample. In fact, these results are comparable to other works using a similar DNN architecture. For instance, Kalvankar et al. (2020) found 92.58% in accuracy for E and S classification, while Cheng et al. (2020) found 99% in 2,800 DES sample and Farias et al. (2020) found $\sim 98\%$ in a SDSS sample of jpg images. In Kalvankar et al. (2020) an extensive multiclass classification is explored. In such a regime, we found more ambiguity between classes and fewer examples per class. For this fine grained classification, it might be the case where more bands could be more advantageous. With fewer examples per class (sometimes orders of magnitude), this is also a regime where ML with morphological features (as the ones from MFMTK), other than DL, could find competitive results. In fact, Figure 11 present how the

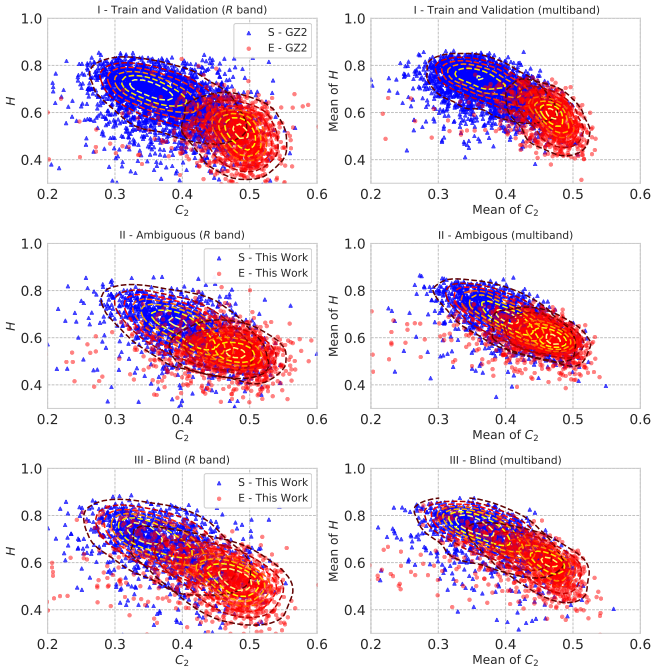

Figure 10. C_2-H diagrams for our three sub-samples (I,II and III). *Left:* only measurements performed in the *r*-band. *Right:* mean value of C_2 and H are computed for each galaxy in different filters (u, g, F515, r, F660, I, F861 and z). The plots are colour coded according to the galaxy classification. The two classes are clearly separated in this plane. Since the E-S classification is trained using GZ1 (i.e. visual classification based on the shape of the object; with or without spiral arms) and the morphometric parameters also measure the monochromatic light distribution, this plot constitutes a sanity check: the two methods recover similarly the form of the objects, without taking into consideration the galaxy colour or stellar population. When considering the mean of C_2 and H across different filters, there is less scatter in the distributions of morphometric indices.

morphological features evolve in different bands in the two groups classified by the method presented in this paper. It is noteworthy the median separation between E and S. The figure presents visual prospect on how the 12 band morphological features could also be exploited for the current binary classification using an algorithm with lower computational complexity, i.e. easily scalable for Big Data regime. We leave this study, including multiclass approach, for a future contribution (Lucatelli et al, in prep.)

7.5 Agreement between Deep Learning classification intuition given in morphological features

The use of DL for imaging recognition extends to way more than astrophysics. Consequently, this method has rapidly advanced and improved in the last years, providing a database for pre-training, ideas and tools that have been largely applied in astronomy, resulting in a wealth of publications (see for example Domínguez Sánchez et al. (2018); Barchi et al. (2020); Tuccillo et al. (2016); Khalifa et al. (2018); Dieleman et al. (2015); Zhu et al. (2019); Dai & Tong (2018)). Barchi et al. (2020) applied Ml and DL techniques to the Sloan Digital Sky Survey Data Release 7 (SDSS-DR7), providing a catalogue of 670,560 galaxies. They achieve a 99% accuracy on average when classifying galaxies into two classes (E's and S's). This result compares well with what obtained in this work, somehow not surprisingly (or maybe reassuring) since they make use of the same training and validation set (i.e. GZ1) and of a similar method, based on DL. To deeply explore the results of these two methods, we can compare Figure 9 of this work with figures 11 and 12 in Barchi et al. (2020). These figures show which T-Type, as obtained by Domínguez Sánchez et al. (2018) and Nair & Abraham (2010), corresponds to E and S galaxies respectively. In theory, E and S0, or early-type galaxies, should have a T-Type ≤ 0, while S, or late-type galaxies, should present a T-Type > 0. On average, both works recover such behaviour, especially when compared with the visual classification of Nair & Abraham (2010) (note that in this work the number statistics in this comparison are lower than in Barchi et al. 2020). Interestingly, when comparing with the automated classification of Domínguez Sánchez et al. (2018), it is clear that in this work the E galaxies class is better defined (i.e. there are almost no galaxies classified as E with a T-Type > 0). Barchi et al. (2020) obtains a similar result when selecting only galaxies with a low probability of being S0 galaxies (as defined in Domínguez Sánchez et al. (2018)). The novel DL algorithm presented in this work is extremely accurate in identifying E galaxies. On the other side, some of the galaxies classified as S have a T-Type ≤ 0 in Domínguez Sánchez et al. (2018), maybe caused by contamination from S0 galaxies. It is hard to compare these results since no code carries the truth, but it is interesting to notice that the main cause of confusion in both the classifications is generally occurring for T-Type $\simeq 0$ (i.e., where the S0 class lies). In this work, as in previous works (Bamford et al. 2009; Lintott et al. 2008, 2010), S0 galaxies are incorporated to the early-type galaxy class, together with the E galaxies, since both classes of objects do not present spiral arms. Yet, low resolution or faint images of S galaxies can be easily misclassified as S0 galaxies and, therefore, as early-type galaxies. A morphological classification that explicitly considers this third group of objects is necessary to overcome this problem (Lucatelli et al in prep).

7.6 Future challenges for Deep Learning morphological classification

Despite the high performance results, there still open challenges for the DL approach in morphological classification. In particular, DNNs are known to find non trivial solutions which might be hard to interpret (Ribeiro et al. 2016; Lundberg & Lee 2017). Thus, it is worth exploring the behaviour of such DNN approach in the survey limits, i.e., in the faint and high redshift end, where humans or measurable morphological features fail, to see if and how the DNN could contribute beyond what one would expect. Other major challenge is to explore the range of small Petrosian radius.

This method will subsequently be applied to the whole S-PLUS survey, providing a morphological classification of galaxies for 8000 deg^2 of the southern hemisphere. Combining galaxy morphology with other data products of the S-PLUS survey, such as stellar population properties, as obtained through SED fitting of the 5 broad and 7 narrow bands, as well as environment measures, recovered via the precise photo-z determinations ($\delta z \simeq 0.03$), will allow to map the large scale structure of the local Universe and probe the dependence on mass and environment of galaxy evolution. Our results enhance the use of pre-trained weights. Presently, due to ImageNet use, we limit the pre-training to the 3-band case. However, as we produced models in multiband datasets, one could use those results in the advantage of pre-trained models for transfer learning using more than three bands in other surveys such LSST (LSST Sci. Collaboration et al. 2009), Euclid (Laureijs et al. 2011), Nancy Grace Roman Space Telescope (Gehrels & and 2015) among oth-

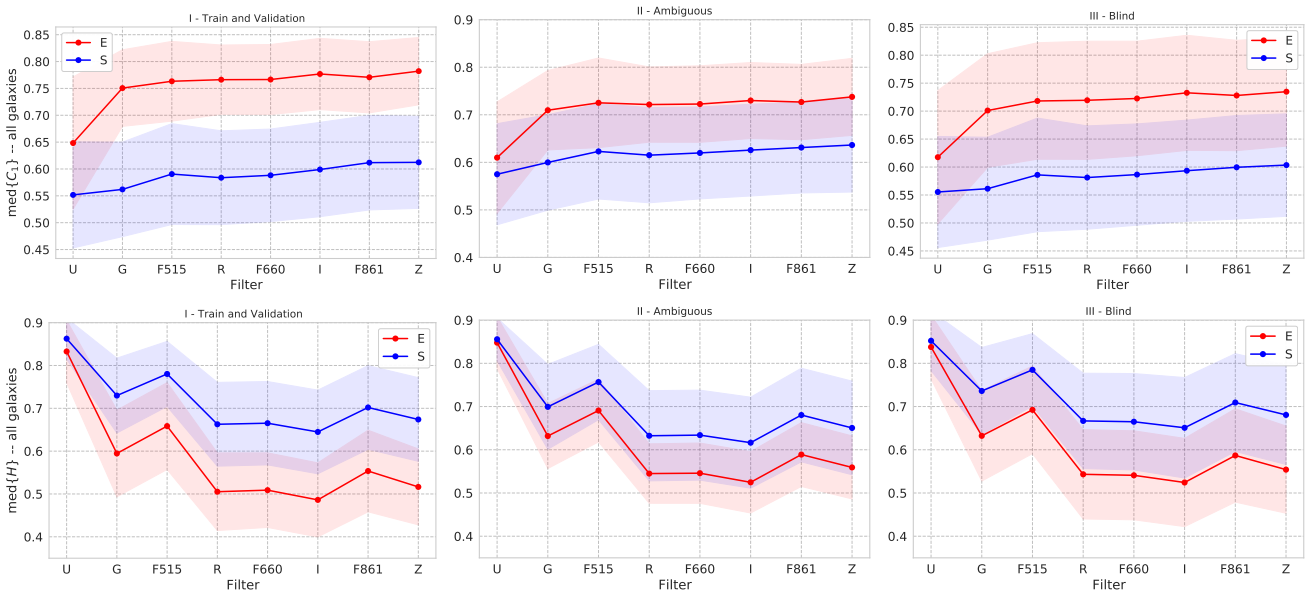

Figure 11. Evolution of morphometric measurements in different filters. These are the median values for H and C_1 for all galaxies in each filter, and the shadowed errors are $\pm 1\sigma$.

ers. In particular, the 8 narrow band model could be used as a starting point for narrow band surveys such as J-PAS (Benitez et al. 2014) and J-PLUS (Cenarro et al. 2019b). By using the current pre-trained models in those surveys it would be possible to evaluate if pre-training in more bands can achieve a gain in a different range of magnitudes and redshifts. Thus, we release out DL models along with our catalogue as a value-added product for the astronomical community.

DATA AVAILABILITY

We make the morphological catalogues developed in this contribution publicly available in https://github.com/cdebom/splus_morph. The Deep Learning models are also public and can be downloaded in http://clearnightsrthebest.com.

ACKNOWLEDGEMENTS

The S-PLUS project, including the T80-South robotic telescope and the S-PLUS scientific survey, was founded as a partnership between the Fundação de Amparo à Pesquisa do Estado de São Paulo (FAPESP), the Observatório Nacional (ON), the Federal University of Sergipe (UFS), and the Federal University of Santa Catarina (UFSC), with important financial and practical contributions from other collaborating institutes in Brazil, Chile (Universidad de La Serena), and Spain (Centro de Estudios de Física del Cosmos de Aragón, CEFCA). We further acknowledge financial support from the São Paulo Research Foundation (FAPESP), the Brazilian National Research Council (CNPq), the Coordination for the Improvement of Higher Education Personnel (CAPES), the Carlos Chagas Filho Rio de Janeiro State Research Foundation (FAPERJ), and the Brazilian Innovation Agency (FINEP).

The authors who are members of the S-PLUS collaboration are grateful for the contributions from CTIO staff in helping in the construction, commissioning and maintenance of the T80-South telescope and camera. We are also indebted to Rene Laporte and INPE, as well as Keith Taylor, for their important contributions to the project. From CEFCA, we particularly would like to thank Antonio Marín-Franch for his invaluable contributions in the early phases of the project, David Cristóbal-Hornillos and his team for their help with the installation of the data reduction package JYPE version 0.9.9, César Íñiguez for providing 2D measurements of the filter transmissions, and all other staff members for their support with various aspects of the project.

CMdO and LSJ acknowledge funding for this work from FAPESP grants 2019/26492-3, 2019/11910-4, 2019/10923-5 and 2009/54202-8. GS, CMdO and LS acknowledge support, respectively, from CNPq grants 309209/2019-6, 115795/2020-0 and 304819/201794. NM acknowledges the University of São Paulo PUB grant 83-1 of 2020. A. C. acknowledge the financial support provided by CAPES.

The authors made use of multi GPU Sci-Mind machines developed and tested for Artificial Intelligence and would like to thank P. Russano and P. Souza Pereira for all the support in infrastructure matters. The authors would like to thank R. C. T. de Souza, C.E. Barbosa, A. L. CHIES-SANTOS, H.Farias, D.Ortiz, M.Jaque Arancibia for useful suggestions and comments.

This paper also made use of the Plot Deep Design [6] library to make plots of the presented architecture.

The authors made use and acknowledge TOPCAT [7] tool to analyse the data.

[6] https://github.com/cdebom/plot_deep_design
[7] http://www.starlink.ac.uk/topcat/(TOPCAT)

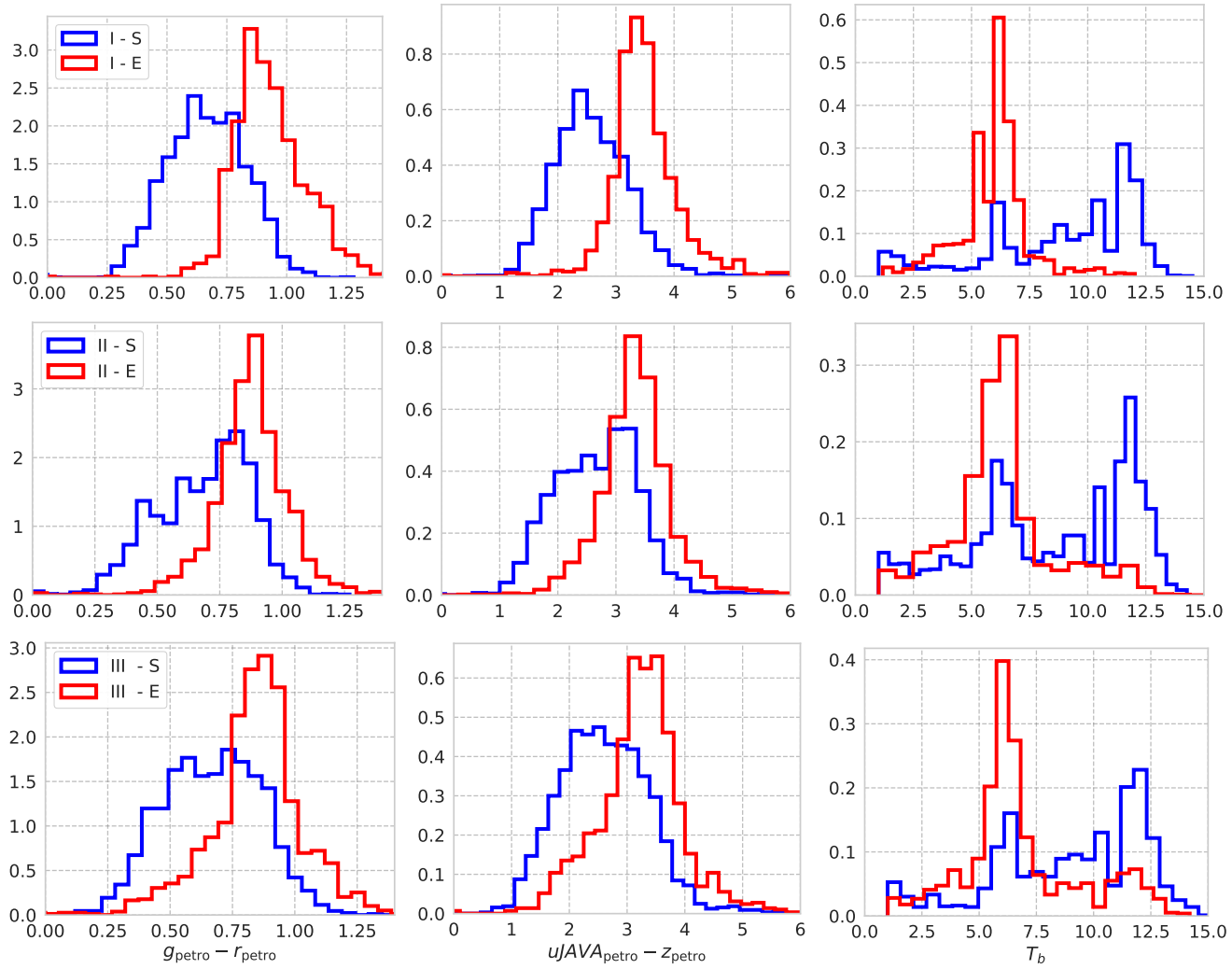

Figure 12. Histogram of the uJAVA-z, g-r and Tb parameters for the E and S training-validation sample (I), the ambiguous sample (II) and the blind sample (III).

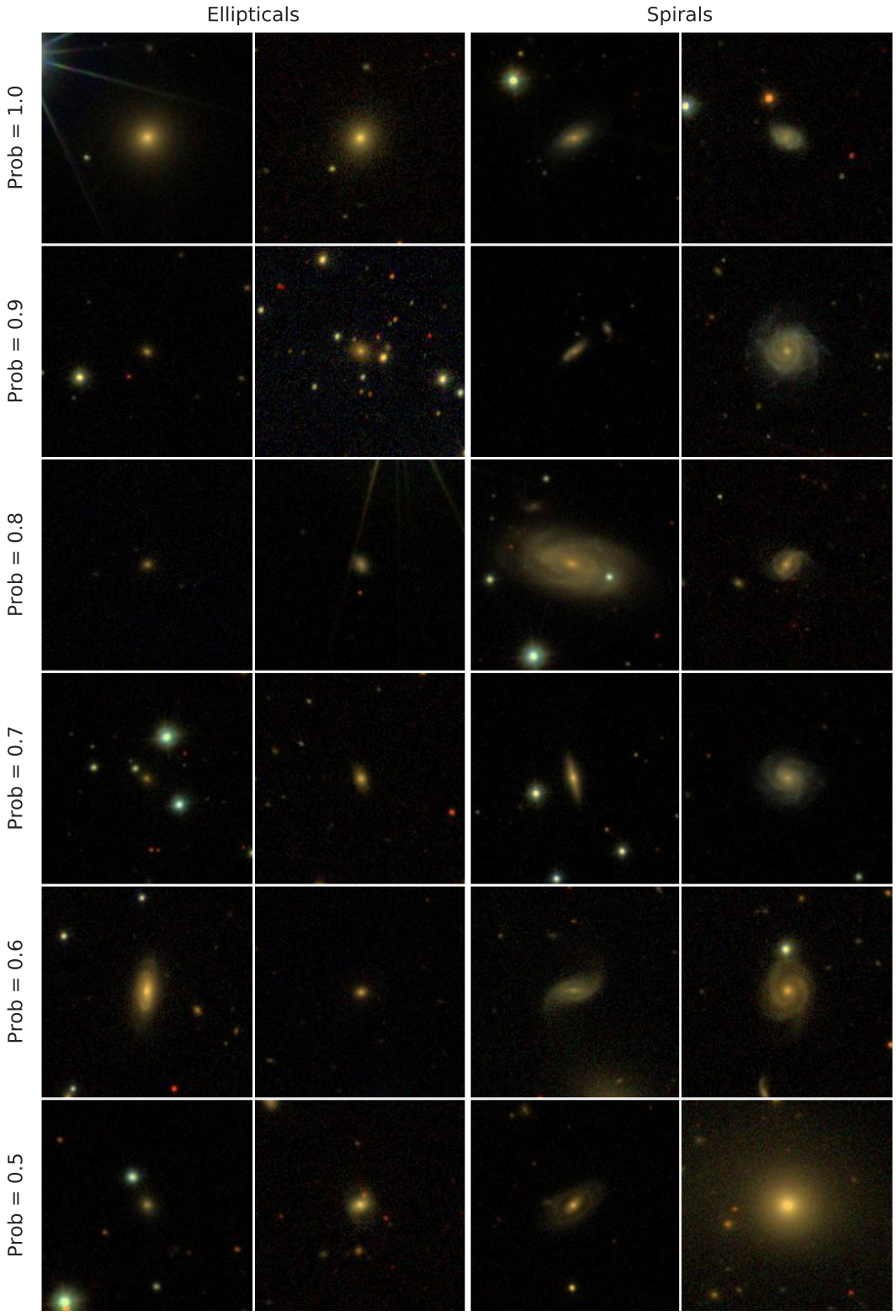

Figure 13. From top to bottom: Example of galaxies images as classified in this work, for decreasing values (from 1 to 0.5) of probability of being spiral (first and second columns) and elliptical galaxies (third and forth column).

REFERENCES

Abdel-Hamid O., Mohamed A.-r., Jiang H., Deng L., Penn G., Yu D., 2014, IEEE/ACM Transactions on audio, speech, and language processing, 22, 1533

Ann H. B., Seo M., Ha D. K., 2015, Astrophys. J. Suppl., 217, 27

Axelrod T. S., 2006, in Gabriel C., Arviset C., Ponz D., Enrique S., eds, Astronomical Society of the Pacific Conference Series Vol. 351, Astronomical Data Analysis Software and Systems XV. p. 103

Bamford S. P., et al., 2009, Monthly Notices of the Royal Astronomical Society, 393, 1324

Banerji M., et al., 2010, Mon. Not. Roy. Astron. Soc., 406, 342

Barchi P. H., et al., 2020, Astronomy and Computing, 30, 100334

Benítez N., 2011, BPZ: Bayesian Photometric Redshift Code (ascl:1108.011)

Benitez N., et al., 2014, arXiv e-prints,

Bernardi M., Domínguez Sánchez H., Brownstein J. R., Drory N., Sheth R. K., 2019, Mon. Not. Roy. Astron. Soc., 489, 5633

Bershady M. A., Jangren A., Conselice C. J., 2000, The Astronomical Journal, 119, 2645

Bishop C. M., 2007, Pattern Recognition and Machine Learning, 1st ed. 2006. corr. 2nd printing edn. Information science and statistics, Springer

Bom C. R., Furlanetto C., More A., Brandt C., Makler M., Santiago B., 2015, in Rosquist K., ed., Thirteenth Marcel Grossmann Meeting: On Recent Developments in Theoretical and Experimental General Relativity, Astrophysics and Relativistic Field Theories. pp 2088–2090, doi:10.1142/9789814623995_0364

Bom C. R., Makler M., Albuquerque M. P., Brand t C. H., 2017, Astr. & Astroph., 597, A135

Borne K. D., et al., 1999, Ap&SS, 266, 137

Cai M. X., Bédorf J., Saletore V. A., Codreanu V., Podareanu D., Chaibi A., Qian P. X., 2020, arXiv e-prints, p. arXiv:2010.11630

Calvi R., Poggianti B. M., Fasano G., Vulcani B., 2012, Mon. Not. Roy. Astron. Soc., 419, L14

Camps-Fariña A., Sanchez S. F., Lacerda E. A. D., Carigi L., García-Benito R., Mast D., Galbany L., 2020, arXiv e-prints, p. arXiv:2011.01229

Cardamone C., et al., 2009, Mon. Not. Roy. Astron. Soc., 399, 1191

Cenarro A. J., et al., 2019a, Astr. & Astroph., 622, A176

Cenarro A. J., et al., 2019b, Astronomy & Astrophysics, 622, A176

Cheng T.-Y., Li N., Conselice C. J., Aragón-Salamanca A., Dye S., Metcalf R. B., 2019, arXiv e-prints, p. arXiv:1911.04320

Cheng T.-Y., et al., 2020, Mon. Not. Roy. Astron. Soc., 493, 4209

Choi K., Fazekas G., Sandler M., Cho K., 2017, in 2017 IEEE International Conference on Acoustics, Speech and Signal Processing (ICASSP). pp 2392–2396

Chollet F., 2018, Deep Learning mit Python und Keras: Das Praxis-Handbuch vom Entwickler der Keras-Bibliothek. MITP-Verlags GmbH & Co. KG

Clarke A. O., Scaife A. M. M., Greenhalgh R., Griguta V., 2020, Astr. & Astroph., 639, A84

Conselice C. J., 2014, Ann. Rev. Astron. Astrophys., 52, 291

Crossett J. P., Pimbblet K. A., Stott J. P., Jones D. H., 2014, Mon. Not. Roy. Astron. Soc., 437, 2521

Dai J.-M., Tong J., 2018, arXiv preprint arXiv:1807.10406

Deng J., Dong W., Socher R., Li L.-J., Li K., Fei-Fei L., 2009, in 2009 IEEE conference on computer vision and pattern recognition. pp 248–255

Dieleman S., Willett K. W., Dambre J., 2015, Monthly notices of the royal astronomical society, 450, 1441

Domínguez Sánchez H., Huertas-Company M., Bernardi M., Tuccillo D., Fischer J. L., 2018, Mon. Not. Roy. Astron. Soc., 476, 3661

Edelen D. G. B., 1969, Ap&SS, 3, 56

Farias H., Ortiz D., Damke G., Jaque Arancibia M., Solar M., 2020, Astronomy and Computing, 33, 100420

Ferrari F., de Carvalho R. R., Trevisan M., 2015, The Astrophysical Journal, 814, 55

Ferreira L., Ferrari F., Griffiths A., 2017, galclean: v1.0.0, doi:10.5281/zenodo.4004571

Forbes D. A., Spitler L. R., Strader J., Romanowsky A. J., Brodie J. P., Foster C., 2011, Mon. Not. Roy. Astron. Soc., 413, 2943

Freeman P. E., Izbicki R., Lee A. B., Newman J. A., Conselice C. J., Koekemoer A. M., Lotz J. M., Mozena M., 2013, Mon. Not. Roy. Astron. Soc., 434, 282

Gehrels N., and D. S., 2015, Journal of Physics: Conference Series, 610, 012007

Glazebrook K., Jacobs C., Collett T., More A., McCarthy C., 2017, Monthly Notices of the Royal Astronomical Society, 471, 167

Glorot X., Bengio Y., 2010, in Proceedings of the thirteenth international conference on artificial intelligence and statistics. pp 249–256

Goodfellow I., Bengio Y., Courville A., 2016, Deep Learning. MIT Press

Gupta R., Srijith P. K., Desai S., 2020, arXiv e-prints, p. arXiv:2012.07735

Hannun A. Y., Rajpurkar P., Haghpanahi M., Tison G. H., Bourn C., Turakhia M. P., Ng A. Y., 2019, Nature medicine, 25, 65

Hausen R., Robertson B. E., 2020, The Astrophysical Journal Supplement Series, 248, 20

He K., Zhang X., Ren S., Sun J., 2016, in Proceedings of the IEEE conference on computer vision and pattern recognition. pp 770–778

Herschel J. F. W., 1864, Philosophical Transactions of the Royal Society of London Series I, 154, 1

Holincheck A. J., et al., 2016, Mon. Not. Roy. Astron. Soc., 459, 720

Howard A. G., Zhu M., Chen B., Kalenichenko D., Wang W., Weyand T., Andreetto M., Adam H., 2017, arXiv preprint arXiv:1704.04861

Hubel D. H., Wiesel T. N., 1962, The Journal of physiology, 160, 106

Huertas-Company M., Rouan D., Tasca L., Soucail G., Le Fèvre O., 2008, Astr. & Astroph., 478, 971

Jacobs C., Glazebrook K., Collett T., More A., McCarthy C., 2017, Monthly Notices of the Royal Astronomical Society, 471, 167

Jacobs C., et al., 2019, Mon. Not. Roy. Astron. Soc., 484, 5330

Kalvankar S., Pandit H., Parwate P., 2020, arXiv e-prints, p. arXiv:2008.13611

Kelly B. C., McKay T. A., 2004, Astron. J., 127, 625

Kent S. M., 1985, Astrophysical Journal, Supplement Series, 59, 115

Khalifa N. E., Taha M. H., Hassanien A. E., Selim I., 2018, in 2018 International Conference on Computing Sciences and Engineering (ICCSE). pp 1–6

Kingma D. P., Ba J., 2014, arXiv preprint arXiv:1412.6980

Knabel S., et al., 2020, Astron. J., 160, 223

Kormendy J., Fisher D. B., Cornell M. E., Bender R., 2009, Astrophys. J. Suppl., 182, 216

Krizhevsky A., Sutskever I., Hinton G. E., 2012, in Advances in neural information processing systems. pp 1097–1105

LSST Sci. Collaboration et al., 2009, arXiv:0912.0201,

Land K., et al., 2008, Mon. Not. Roy. Astron. Soc., 388, 1686

Lanusse F., Ma Q., Li N., Collett T. E., Li C.-L., Ravanbakhsh S., Mandelbaum R., Póczos B., 2018a, Mon. Not. Roy. Astron. Soc., 473, 3895

Lanusse F., Ma Q., Li N., Collett T. E., Li C.-L., Ravanbakhsh S., Mandelbaum R., Póczos B., 2018b, Mon. Not. Roy. Astron. Soc., 473, 3895

Laureijs R., et al., 2011, arXiv e-prints, p. arXiv:1110.3193

LeCun Y., Bottou L., Bengio Y., Haffner P., et al., 1998, Proceedings of the IEEE, 86, 2278

LeCun Y., Bengio Y., Hinton G., 2015, nature, 521, 436

Li X., Ding Q., Sun J.-Q., 2018, Reliability Engineering and System Safety, 172, 1

Lintott C. J., et al., 2008, Monthly Notices of the Royal Astronomical Society, 389, 1179

Lintott C., et al., 2010, Monthly Notices of the Royal Astronomical Society, 410, 166

Liu L., Jiang H., He P., Chen W., Liu X., Gao J., Han J., 2019, arXiv, pp arXiv–1908

Lu J., Wang G., Zhou J., 2017, IEEE Transactions on Image Processing, 26, 4042

Lundberg S. M., Lee S.-I., 2017, in Advances in neural information processing systems. pp 4765–4774

Ma Z., et al., 2019, Astrophys. J. Suppl., 240, 34

Madireddy S., Li N., Ramachandra N., Balaprakash P., Habib S., 2019,

Modular Deep Learning Analysis of Galaxy-Scale Strong Lensing Images (arXiv:1911.03867)
Mendes de Oliveira C., et al., 2019, Monthly Notices of the Royal Astronomical Society, 489, 241
Metcalf R. B. e. a., 2021, in preparation
Metcalf R. B., et al., 2019, Astronomy & Astrophysics, 625, A119
Molino A., et al., 2020, Mon. Not. Roy. Astron. Soc., 499, 3884
Moreno-Torres J. G., Sáez J. A., Herrera F., 2012, IEEE Transactions on Neural Networks and Learning Systems, 23, 1304
Naab T., Johansson P. H., Ostriker J. P., 2009, Astrophys. J. Lett., 699, L178
Nair P. B., Abraham R. G., 2010, Astrophys. J. Suppl., 186, 427
Ostrovski F., et al., 2017, Mon. Not. Roy. Astron. Soc., 465, 4325
Peng C. Y., Ho L. C., Impey C. D., Rix H.-W., 2002, Astron. J., 124, 266
Petrillo C. E., et al., 2019a, Mon. Not. Roy. Astron. Soc., 482, 807
Petrillo C. E., et al., 2019b, Mon. Not. Roy. Astron. Soc., 484, 3879
Pović M., et al., 2015, Mon. Not. Roy. Astron. Soc., 453, 1644
Ribeiro M. T., Singh S., Guestrin C., 2016, arXiv preprint arXiv:1606.05386
Ruder S., 2016, arXiv preprint arXiv:1609.04747
Russakovsky O., et al., 2015, International Journal of Computer Vision (IJCV), 115, 211
Sánchez S. F., Cardiel N., Verheijen M. A. W., Pedraz S., Covone G., 2007, Mon. Not. Roy. Astron. Soc., 376, 125
Sarkar S., Pandey B., 2020, Mon. Not. Roy. Astron. Soc., 497, 4077
Shamir L., Holincheck A., Wallin J., 2013, Astronomy and Computing, 2, 67
Shao X., Disseau K., Yang Y. B., Hammer F., Puech M., Rodrigues M., Liang Y. C., Deng L. C., 2015, Astr. & Astroph., 579, A57
Simmons B. D., et al., 2017, Mon. Not. Roy. Astron. Soc., 464, 4420
Simonyan K., Zisserman A., 2014, arXiv preprint arXiv:1409.1556
Slosar A., White M., 2009, JCAP , 2009, 009
Spiekermann G., 1992, Astron. J., 103, 2102
Storrie-Lombardi M. C., Lahav O., Sodre L., Storrie-Lombardi L. J., 1992, Mon. Not. Roy. Astron. Soc., 259, 8
Sun Y., Wong A. K., Kamel M. S., 2009, International journal of pattern recognition and artificial intelligence, 23, 687
Szegedy C., et al., 2015, in Proceedings of the IEEE conference on computer vision and pattern recognition. pp 1–9
Szegedy C., Vanhoucke V., Ioffe S., Shlens J., Wojna Z., 2016, in Proceedings of the IEEE conference on computer vision and pattern recognition. pp 2818–2826
Tan M., Le Q., 2019, in International Conference on Machine Learning. pp 6105–6114
Tan M., Chen B., Pang R., Vasudevan V., Sandler M., Howard A., Le Q. V., 2019, in Proceedings of the IEEE Conference on Computer Vision and Pattern Recognition. pp 2820–2828
Tuccillo D., Decencière E., Velasco-Forero S., et al., 2016, Proceedings of the International Astronomical Union, 12, 191
Tyson J. A., 2002, in Tyson J. A., Wolff S., eds, Society of Photo-Optical Instrumentation Engineers (SPIE) Conference Series Vol. 4836, Survey and Other Telescope Technologies and Discoveries. pp 10–20 (arXiv:astro-ph/0302102), doi:10.1117/12.456772
Vaucouleurs G., 1959, Handbuch der Physik, 11, 275
Vecchiotti P., Vesperini F., Principi E., Squartini S., Piazza F., 2018, in , Multidisciplinary Approaches to Neural Computing. Springer, pp 161–170
Vega-Ferrero J., et al., 2020, arXiv e-prints, p. arXiv:2012.07858
Walmsley M., et al., 2020, Mon. Not. Roy. Astron. Soc., 491, 1554
Wang B., Cappellari M., Peng Y., Graham M., 2020, Mon. Not. Roy. Astron. Soc., 495, 1958
Willett K. W., et al., 2013, Mon. Not. Roy. Astron. Soc., 435, 2835
Wjeisinghe D. B., Hopkins A. M., Kelly B. C., Welikala N., Connolly A. J., 2010, Mon. Not. Roy. Astron. Soc., 404, 2077
Wu J. F., 2020, Astrophys. J., 900, 142
Wu C., et al., 2019, Mon. Not. Roy. Astron. Soc., 482, 1211
Yamauchi C., et al., 2005, Astron. J., 130, 1545
York D. G., et al., 2000, Astron. J., 120, 1579
Yosinski J., Clune J., Bengio Y., Lipson H., 2014, in Advances in neural information processing systems. pp 3320–3328
Zagoruyko S., Komodakis N., 2016, arXiv preprint arXiv:1605.07146
Zhu X.-P., Dai J.-M., Bian C.-J., Chen Y., Chen S., Hu C., 2019, Astrophysics and Space Science, 364, 55
Zwicky F., 1940, Physical Review, 58, 478
de Albernaz Ferreira L., Ferrari F., 2018, Mon. Not. Roy. Astron. Soc., 473, 2701
de la Calleja J., Fuentes O., 2004, Mon. Not. Roy. Astron. Soc., 349, 87
van den Bergh S., 1998, Galaxy Morphology and Classification, 1st ed. 1998 edn. Cambridge University Press